Planetary Circulations: 2. The Jovian Quasi-Geostrophic Regime

GARETH P. WILLIAMS

Geophysical Fluid Dynamics Laboratory/NOAA, Princeton University, Princeton, NJ 08540

(Manuscript received 12 September 1978, in final form 30 January 1979)

ABSTRACT

The characteristics of the two-level quasi-geostrophic model are evaluated for a wide range of parameter values in the Jovian domain. The results support the hypothesis that baroclinic instability energizes the circulation of Jupiter and Saturn and that the blocking effect of planetary wave propagation on quasi-geostrophic turbulent cascades determines the width and zonality of the bands—the degree of zonality being higher in the absence of surface drag.

The model circulations consist of multiple westerly jets, separated by strong easterly flows—the result of momentum partitioning by the Kuo vortex separation process. There are no large-scale vertical motions. A cyclic variation occurs (with a time scale of several years) during which phases with intense, large-scale baroclinic activity alternate with longer, more quiescent phases involving weak, small-scale baroclinic instability and neutral baroclinic waves. These neutral waves, generated by quasi-two-dimensional cascades and propagating at speeds of O(1 m s^{-1}), provide the major mode of adjustment in the quasi-steady phase and form the gyres endemic to multiple jet circulations.

Similar large-scale motions occur for all the parameter values considered: for weak and strong static-stabilities, for eddy sizes ranging from 2000–9500 km and for pole-to-equator temperature differences varying from 5–90 K. The weak thermal gradients maintain strong dynamical activity by their association, in geostrophic motion, with the large value of the specific-heat constant for hydrogen.

For Jupiter, a correspondence between the theoretical perturbation pressure and the observed planetary-scale features suggests that condensation processes related to the geostrophically balanced pressure variations produce the main cloud bands and Great Red Spot, while local temperature changes due to baroclinic instability and frontogenesis create the eddy cloud systems embedded within the main bands. An analogy between the Great Red Spot and the warm high-pressure region of a neutral baroclinic wave leads us to suggest that the scale selectivity and energy source of ultralong, baroclinically unstable waves could explain the size and persistence of the Jovian feature.

1. Introduction

To help isolate the formative processes of the planetary circulations of Jupiter and Saturn, we continue our evaluation of the behavior, under Jovian conditions, of mechanisms known to be important in the Earth's atmosphere. The solutions in Part 1 (Williams, 1978) showed that zonally banded forms of circulation, composed of multiple easterly and westerly jets, arise in a quasi-barotropic model of a rapidly rotating atmosphere when two-dimensional turbulent cascades, driven by pseudo-baroclinic eddies, interact with Rossby-wave propagation. The flows resemble that on Jupiter most closely when the scale of the eddies is comparable to that of the jets—such eddies could be produced by baroclinic instability. To determine whether multi-jet circulations can occur under *realistic* planetary conditions requires that we now examine their generation in a *deterministic* model with self-regulating energy sources.

The two-level quasi-geostrophic approximation (Phillips, 1956) provides the simplest circulation model appropriate to this task. With it, the characteristics of quasi-geostrophic turbulence—particularly the dependence of multiple-jet formation and equilibration on the temporal and spatial scales of energy conversion—can be evaluated in the Jovian parameter range and possible analogies with the planetary circulation examined.[1] The unwarranted belief that the circulations of Jupiter and Earth differ fundamentally in their dynamics (because of the pseudo-axisymmetry of the former)—a difference that would invalidate the relevance of the quasi-geostrophic approximation to Jupiter—is due to a parameterically limited understanding of the nonlinear responses of this model.

The characteristic responses of the two-level model, as revealed by linear analysis, assist in designing and in interpreting the calculations. In particular, normal-mode studies (Phillips, 1954; Stone, 1969; Simmons, 1974) indicate that in quasi-geostrophic circulations, the

[1] To distinguish between planet and model, the term "Jovian regime" will be used when referring to the latter.

baroclinic eddies should be equal in size to the Rossby radius of deformation L_ρ in the longitudinal direction and to the geometric mean of L_ρ and $L_{\bar{u}}$ (a scale inherent in the curvature of the mean zonal flow) in the latitudinal direction. This result applies to the eddy-free phases of the flow, but not to the turbulent phases where the scale $L_{\bar{u}}$ is determined *by* the eddy characteristics, rather than vice versa.[2]

Theory, however, does not place any binding constraints on the value of the unknown parameters, such as the static stability. Global integration of the two-level model, using parameterizations of eddy heat flux based on instability theory, gives an estimate of the contribution of baroclinic eddies to the mean static stability: 10^{-3} K km^{-1} for Jupiter (Stone, 1972). Unfortunately, such estimates do not provide any real measure of the planetary lapse rate because cloud and convection effects also play a major role in determining the atmospheric parameter, both on Earth (e.g., Schneider and Dickinson, 1974) and Jupiter. Furthermore, the theoretical assumptions fail in the Jovian regime, where—because the barotropic component so greatly exceeds the baroclinic—the nonlinear exchanges differ from their terrestrial forms.

The relevance of the two-level model to a deep atmosphere depends mainly on the vertical variation of the static stability. If the vertical structure of Jupiter's circulation resembles that of the ocean where activity decays exponentially with depth, only a minor modification of the baroclinic characteristics, as represented by the two-level model, occurs (Gill *et al.*, 1974; Williams, 1974). If a baroclinic layer behaves in the same way as McIntyre's (1972) stratospheric model, significant energy could be lost to lower layers (Stone, 1976); but, for this to occur requires that the fluid have a singular vertical structure, not typical of the ocean or a deep atmosphere [see Philander (1978), Eq. (20)].

Observations of Jupiter relate mainly to the quasi-barotropic features of the circulation. Nothing definitive is known about the baroclinic or vertical aspect of the atmosphere. Experimental and theoretical uncertainties in interpreting spacecraft measurements undermine all attempts to estimate the planet's thermal structure. Any inferences made about the meridional temperature variation—such as the view that Jupiter has no baroclinicity—are quite arbitrary. Thus, there is no conflict with the theory to be presented.

2. The quasi-geostrophic model

The two-level quasi-geostrophic β-plane model describes the approximate behavior of the largest scales of motion in a rotating planetary atmosphere. The governing equations, derived by Phillips (1956, 1963) and Pedlosky (1964), are reviewed in this section; a reformulation of the numerical scheme, boundary conditions and diagnostic equations is given in Appendix A.

List of Symbols

We adopt the following standard notation for β-plane flow:

x	prograde distance coordinate (toward east)
y	northward distance coordinate
p	pressure (the vertical coordinate)
t	time
u, v, ω	time rate of change of x, y, p following the motion
$\mathbf{V}$	horizontal velocity vector
U	rms velocity scale
θ	latitude
Θ	potential temperature
Φ	geopotential [$=gz$ where z is height]
f	Coriolis term [$=2\Omega\sin\theta$]
f_0	Coriolis term at mean latitude θ_0 [$=2\Omega\sin\theta_0$]
β	Rossby parameter [$=2\Omega\cos\theta_0/a$]
a	planetary radius
Ω	planetary rotation rate
g	acceleration of gravity
R	specific gas constant
c_p	specific heat at constant pressure
T	temperature
ΔT	temperature difference between pole and equator on p_2 isobar
ν	horizontal small-scale diffusion coefficient
$\dot{Q}$	non-adiabatic heating rate per unit mass.
H	non-adiabatic heating rate function [$=R\dot{Q}/c_p$]
h	scale height [$=RT_0/g$]
p_2	pressure at mass center of dynamic layer
p_4	pressure at bottom of active layer
Δp	pressure grid interval [$=p_4-p_2$]
γ^2	inverse static stability parameter {$=\Theta_2[(\Phi_1-\Phi_3)(\Theta_1-\Theta_3)]^{-1}$, assumed constant}
λ^2	Froude parameter [$=f_0^2\gamma^2$, where λ^{-1} is the Rossby radius of deformation]
τ_D	time scale of surface (Ekman layer) drag
τ_I	time scale of interface drag
q	potential vorticity
ζ	vorticity [$=\nabla^2\psi$]
ψ	geostrophic streamfunction [$u=-\psi_y$, $v=\psi_x$]
∇	horizontal gradient operator on an isobaric surface
w	vertical velocity [assumed$=-h\omega/p_2$]
τ^x, τ^y	x, y components of vertical stress
$(^-)$	zonal mean $\left[=X^{-1}\int_0^X (\,)dx\right]$
$\langle(\,)\rangle$	domain mean $\left[=Y^{-1}\int_0^Y (^-)dy\right]$

[2] $L_{\bar{u}}$ equals $L_\beta[\equiv\pi(2U/\beta)^{\frac{1}{2}}]$, where U is the rms velocity and β the northward gradient of the Coriolis force. (See the discussion of the Rhines effect in Part 1.)

$(\hat{\ })$ baroclinic component $[=(\ )_1-(\ )_3$, difference between values at p_1, p_3 levels]
$(\tilde{\ })$ barotropic component $[=(\ )_1+(\ )_3$, sum of values at p_1, p_3 levels]
$\delta_x A$ differencing operator $\{=[A(x+\Delta x/2)-A(x-\Delta x/2)]/\Delta x\}$
$\overline{(A)}^x$ averaging operator $\{=[A(x+\Delta x/2)+A(x-\Delta x/2)]/2\}$
Δt time step
n number of time steps.

a. The basic equations

In the quasi-static, quasi-geostrophic approximation, the equations of motion, thermodynamic energy and mass conservation are

$$u_t+\mathbf{V}\cdot\nabla u-(fv)^*=-\Phi_x^*+\nu\nabla^2 u+g\tau_p^x, \quad (1)$$

$$v_t+\mathbf{V}\cdot\nabla v+(fu)^*=-\Phi_y^*+\nu\nabla^2 v+g\tau_p^y, \quad (2)$$

$$(\ln\Theta)_t+\mathbf{V}\cdot\nabla(\ln\Theta)+\omega(\ln\Theta)_p=\dot{Q}/c_pT, \quad (3)$$

$$\nabla\cdot\mathbf{V}^*+\omega_p=0, \quad (4)$$

where the asterisk denotes quantities accurate to first order in Rossby number, the other quantities being zero-order (quasi-geostrophic) terms.

The continuously varying atmosphere is replaced by one consisting of two layers in which the horizontal velocities and pressure forces are independent of height. Quantities are defined at pressure levels denoted by p_k $(k=0, 4)$, where the subscript indicates the level in increments of $\Delta p/2$ from the upper surface (when the two layers are of equal mass). Velocities at the p_1, p_3 levels represent flow in the upper and lower layers, respectively. Evaluation of the thermodynamic equation at the p_2 level excludes prediction of static stability changes and implies that the heating be regarded as a vertically averaged quantity.

The β-plane approximation $f^*=f_0+\beta(y-Y/2)$ is made for fluid occupying a rectangular region $0\leqslant x\leqslant X$, $0\leqslant y\leqslant Y$, centered on midlatitudes, with periodicity in x and impermeability on latitudinal vertical walls whose distance apart equals the planetary pole-to-equator span. Then, assuming a vertical boundary condition $\omega=0$ on p_0 and p_4, a constant static-stability factor $\gamma^2>0$, the validity of the quasi-geostrophic approximation $\Phi=f_0\psi$, and linear stress forms with time scales τ_D and τ_I, it follows that the primitive equations can be written in the following vorticity form (on taking the curl) and the thermodynamic energy equation in quasi-static form:

$$\zeta_{1t}+\mathbf{V}_1\cdot\nabla(f^*+\zeta_1)-\frac{f_0}{p_2}\omega_2=\nu\nabla^2\zeta_1-\hat{\zeta}/\tau_I, \quad (5)$$

$$\zeta_{3t}+\mathbf{V}_3\cdot\nabla(f^*+\zeta_3)+\frac{f_0}{p_2}\omega_2=\nu\nabla^2\zeta_3+\hat{\zeta}/\tau_I-\zeta_4/\tau_D, \quad (6)$$

$$\frac{w_2}{h}=-\frac{\omega_2}{p_2}=\gamma^2[H-f_0(\hat{\psi}_t+\mathbf{V}_2\cdot\nabla\hat{\psi}-\nu\nabla^2\hat{\psi})], \quad (7)$$

$$\tilde{\mathbf{V}}_{1y}^*=-\tilde{\mathbf{V}}_{3y}^*=-\tilde{\omega}_2/p_2. \quad (8)$$

By eliminating ω_2, the equations can be reduced to the concise potential vorticity forms

$$q_{1t}+\mathbf{V}_1\cdot\nabla(f^*+q_1)=\nu\nabla^2 q_1-f_0\gamma^2H-\hat{\zeta}/\tau_I, \quad (9)$$

$$q_{3t}+\mathbf{V}_3\cdot\nabla(f^*+q_3)=\nu\nabla^2 q_3+f_0\gamma^2H+\hat{\zeta}/\tau_I-\zeta_4/\tau_D, \quad (10)$$

$$q_1=\nabla^2\psi_1-\lambda^2\hat{\psi}, \quad (11)$$

$$q_3=\nabla^2\psi_3+\lambda^2\hat{\psi}. \quad (12)$$

The velocity $\mathbf{V}$ and vorticity ζ terms in (5), (6), (7), (9) and (10) are evaluated from the geostrophic streamfunction. Eq. (8) then gives a higher order (in Rossby number) mean meridional circulation. The quantity $\hat{\psi}$ (evaluated at the p_2 level) provides a measure of hydrostatic temperature change through the relation $T_2=f_0\hat{\psi}/R$ given by the hydrostatic equation $\Phi_p=-RT/p$.

b. Physical assumptions

The heating function H represents the imbalance of the radiative, convective and interior heating sources and specifies the heat that the large-scale motions must redistribute. We regard the static stability as being controlled primarily by the convective and radiative heat transfers, with the baroclinic eddies making only a secondary contribution.

The interaction with the lower regions is represented by a simple drag or Ekman formulation. We use two definitions for the surface vorticity ζ_4:

$$\zeta_4^p=-\tfrac{1}{2}\zeta_1+\tfrac{3}{2}\zeta_3, \quad (13)$$

$$\zeta_4^c=\tfrac{1}{2}\zeta_3, \quad (14)$$

where the first is an extrapolation form (Phillips, 1956) and the second, a layer-localized form (Charney, 1959). The drag time scale is relatively short for Earth ($\tau_D=2.5\times10^5$ s) but apparently lengthy for Jupiter. The term $\hat{\zeta}/\tau_I$ describes the vertical diffusion of momentum across the p_2 interface by small-scale (cumulus) convection. This term appears to have little effect on flow character and is omitted from most calculations.

The lateral diffusion terms are primarily a numerical device to represent subgrid-scale motion and produce meaningful spectra. To reduce the effects of this term on the largest scales and make it more scale selective, we occasionally replace the simple diffusion expression by the form

$$\bar{\nu}\bar{q}_{yy}+\nu'\nabla^2 q', \quad (15)$$

where the coefficient for the zonal mean $\bar{\nu}$ is substantially less than that for the eddies ν'. This modification has no fundamental consequences and proves useful in computationally difficult, weakly energized

flows. For convenience, we write all equations with the standard diffusion formulation.

The selection of the lateral boundary conditions is constrained by, and inseparable from, the use of a finite-difference formulation. Boundary conditions that yield a state of wall-neutrality, and conserve vorticity, momentum, mass and heat are imposed. Appendix A describes the reasons for this choice and the method of solving the prediction and diagnostic equations.

3. Design of experiments

The quasi-geostrophic equations describe time-dependent three-dimensional flow in the multi-parameter space defined by X, Y, f_0, β, γ^2, H, τ_D, τ_I and ν. To evaluate the equations in the planetary context, we must choose values for these parameters appropriate to Jupiter. Few are known, so a "Jovian regime" is defined, in which Y, f_0, β are set at Jupiter's values, while allowing the other parameters to vary arbitrarily.

The values of γ^2, H, τ_D constitute the major unknown items of dynamical significance in the Jovian regime and in the following sections we attempt to place bounds on their magnitudes.

a. Static stability

Given the lack of observational estimates, the static-stability factor γ^2 was chosen empirically to have values lying between 10 and 250 s^2 km^{-2}. These correspond, via the relation

$$\langle\Theta_z\rangle = \Theta_2/g\gamma^2\hat{z}^2, \tag{16}$$

to strong and weak lapse rates of 1 and 10^{-2} K km^{-1}, respectively ($\hat{z}$ is the distance between the p_1 and p_3 levels).

Corresponding to this γ^2 range, the critical baroclinicity needed to activate the baroclinic instability mechanism varies from 40–2 K for the strongly and weakly stable atmospheres, respectively (see Table 1 and Fig. 1). This is according to an analysis (Phillips, 1954) which gives the minimum shear and baroclinicity and the preferred longitudinal length scale for eddy development as

$$\hat{u}_c = \beta/\gamma^2 f_0^2, \quad \Delta T_c = \beta Y/R f_0 \gamma^2, \quad L_c = 2\pi 2^{\frac{1}{2}}/\gamma f_0. \tag{17}$$

TABLE 1. Minimum values of critical length scale, shear and temperature differential as function of γ^2 (after Phillips, 1954), using Jovian values of f_0, β, R (see Table 2) so that $L_c = 3\times10^4/\gamma$ [km], $\hat{u}_c = 60/\gamma^2$ [m s^{-1}], $\Delta T_c = 400/\gamma^2$ [K].

γ^2 (s^2 km^{-2})	L_c (km)	$\hat{u}_c$ (m s^{-1})	ΔT_c (K)
10	9500	6	40
25	6000	2	16
50	4200	1	8
100	3000	0.6	4
250	2000	0.2	2

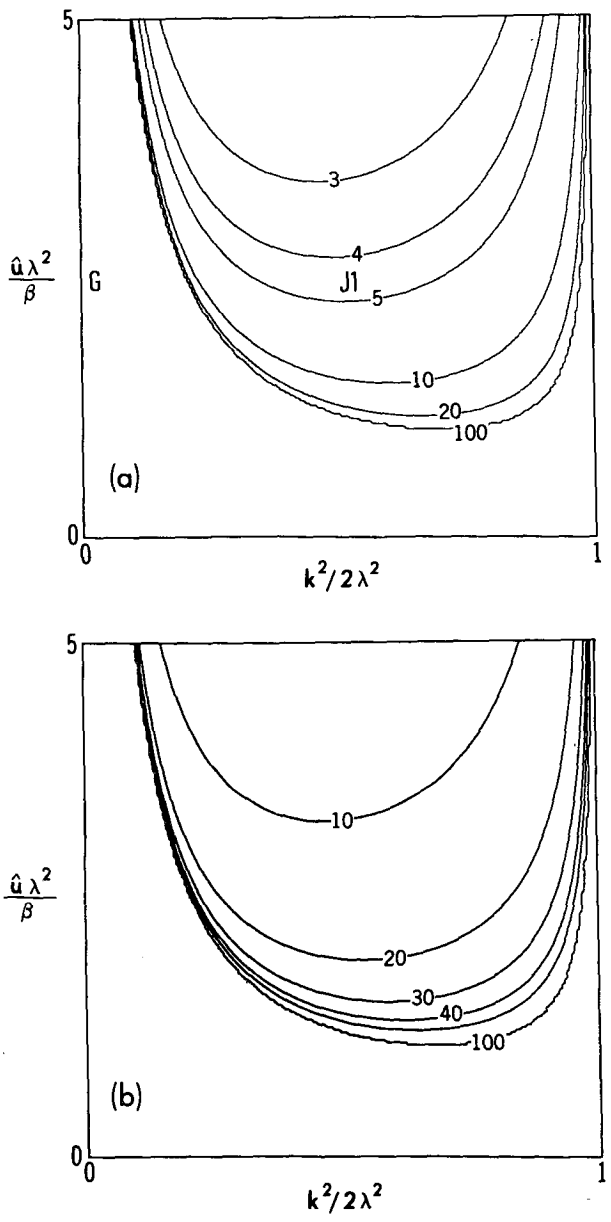

FIG. 1. Instability curves for the two-level model showing time in days for an unstable wave to double its amplitude, as a function of the nondimensional vertical wind shear $\hat{u}\lambda^2/\beta$ versus a nondimensional wavenumber $k^2/2\lambda^2$. Evaluation is for values of $f_0 = 2.5\times10^{-4}$ s^{-1}, $\beta = 0.36\times10^{-8}$ s^{-1} km^{-1} and extremes of static stability (a) $\gamma^2 = 25$ s^2 km^{-2}, (b) $\gamma^2 = 250$ s^2 km^{-2}. J1 and G denote approximate locations of main instabilities and gyres, respectively.

Jupiter's baroclinicity can be estimated from the global heat flux measurements, if we assume that the polar region is heated only by the interior source and the equatorial by both interior and solar sources. The corresponding effective temperatures, 100 and 135 K, give a ΔT of 35 K. This further suggests that, if the criteria of linear theory are relevant, the preferred value of γ^2 is 25 s^2 km^{-2}. Saturn, with its weaker

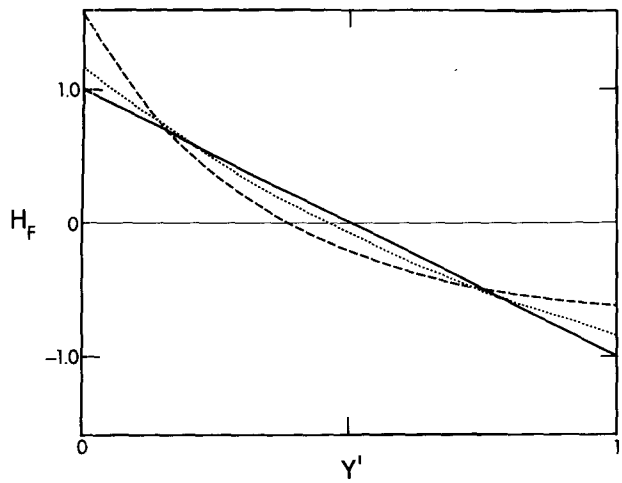

FIG. 2. Form of the heating distribution $H_F(y)$ from equatorial to polar boundaries. Solid curve is standard linear variation, dotted is based on weak exponential function $e^{-y'}$ and dashed on the strong exponential function $e^{-3y'}$ [see Eq. (18)].

interior source, could have $\Delta T=70$ K and $\gamma^2=10$ s^2 km^{-2}.

The upper bound on the static stability factor ($\gamma^2=250$ s^2 km^{-2}) arises because of the computational difficulty in resolving eddies much smaller than the 2000 km scale. The corresponding solution, with a $\Delta T_c\approx 2$ K, indicates that, in a weakly dissipative atmosphere, circulations can occur at very small baroclinicity levels (of the order of errors in the Pioneer 11 effective temperature measurements).

b. Heating distribution

The heat balance of Jupiter's atmosphere cannot be estimated directly because of the unknown distribution of the interior supply. Three important factors disturb any thermodynamic analogy with Earth: the high opacity and long radiative time scale of the hydrogen atmosphere, the complex distribution of clouds and aerosols (Rossow, 1978) and the unknown relaxation time of small-scale convection.

For the model, we examine the response to simple empirical heating functions which are written in the form $H=H_a\cdot H_F(y)$, where H_a is the amplitude and $H_F(y)$ the normalized latitudinal distribution. For the majority of the calculations, the function has the simple linear form $H_F(y)=1-2y'$, $y'=y/Y=0$, 1, corresponding to uniform baroclinicity. However, because circulations are sensitive to the heating distribution, the effects of variable baroclinicity are examined via the simple exponential form

$$H_F(y)=c_1+c_2\exp(-dy'), \tag{18}$$

with $d=1$ and 3 for moderate and strong changes. The constants c_1 and c_2 satisfy the integral constraints

$$\int_0^Y H_F dy=0, \quad \int_0^Y |H_F| dy=0.5$$

for consistency with the linear form (Fig. 2). All functions describe an excess heating in low latitudes and a deficiency in high latitudes.

c. Heating amplitude

Imposing a heating rate on the model is analogous to fixing the static stability and can be misleading if physical constraints are violated. The eddies in the Jovian regime can only transfer a certain amount of heat poleward and cannot cope with excessive heating rates—under which a continual rise in ΔT occurs. Although theoretical estimates of the eddy heat transfer rates can be made, they are not sufficiently accurate; numerical experimentation is preferable.

Estimates of the value of H_a appropriate to Earth give values between 1 and 2 units (a unit being 10^{-9} km^2 s^{-3}); Phillips used $H_a=1.2$ units. In the absence of motion, $H_a=1$ unit produces an equatorial temperature rise of 0.25 K per day in the terrestrial regime and 0.25 K per month in the Jovian regime. Jupiter's atmosphere receives about 1/25 as much solar heat as Earth, together with a comparable amount from the planet's interior, so that a heating rate of 0.1–0.2 units seems appropriate for the model. For computational efficiency and accuracy,[3] a value of $H_a=0.4$ units was used for the initial calculations but solutions indicate that $H_a=0.2$ units is the preferred value for flow equilibration.

The main significance of the heating rate lies in its control of the time scale of events, through its rate of buildup of the critical temperature gradients for instability. Short-term calculations, involving only the instability of the axisymmetric state and the inertial aftermath, do not depend crucially on the value of H_a.

d. Dissipation

The time scale τ_D must exceed the doubling times in Fig. 1 if the drag is not to inhibit baroclinic instability. Experimentation indicates that when $\tau_D\approx 100$ days,[4] the drag makes a primary contribution to the characteristics of the circulation by modifying the zonality of the jets. When $\tau_D\approx 500$ days (the inertial time scale), the drag effect is secondary but sufficient for momentum equilibration. Dissipative time scales are longer for lighter gases: τ_D varies as R (Phillips, 1956). For short-term calculations, the vertical stresses are omitted.

[3] Too small a value of H_a produces small tendencies in the prediction equations. (See Part 1, Appendix Section 8).

[4] In this paper, 1 day equals 86 400 s.

TABLE 2. Jupiter regime cases. Constant parameter values (comparative terrestrial values in parenthesis): $a=0.7\times10^5$ (0.6×10^4) km, $\Omega=0.176\times10^{-3}$ (0.73×10^{-4}) s^{-1}, $R=0.42\times10^{-2}$ (0.29×10^{-3}) $km^2\,s^{-2}\,K^{-1}$, $f_0=0.25\times10^{-3}$ (1.0×10^{-4}) s^{-1}, $\beta=0.36\times10^{-8}$ (0.16×10^{-7}) $s^{-1}\,km^{-1}$, $h=20(8)$ km. L denotes linear distribution. τ_4^c stress term used throughout.

Case	γ^2 (s^2 km^2)	H_a (10^{-9} km^2 s^{-3})	H_F	τ_D (10^5 s)	τ_I (10^5 s)	X (10^3 km)	Y (10^3 km)	Resolution $X/\Delta x$	$Y/\Delta y$	Axisymmetric stage: $\bar{\nu}$ (km^2 s^{-1})	Δt (10^3 s^{-1})	Total time (days)	ΔT (K)	U_1 (m s^{-1})	$\hat{u}_{max}$ (m s^{-1})
J1	25	0.4	L	∞	∞	35	110	128	256	0.02	80	1840	29.4	2.3	4.5
J2	10	1.0	L	∞	∞	60	110	128	128	0.20	170	1564	57.0	4.9	9.8
J3	50	0.4	L	∞	∞	32	110	128	256	0.02	90	1035	16.7	1.3	2.6
J4	100	0.4	L	∞	∞	22	110	128	512	0.01	80	644	10.5	0.8	1.6
J5	250	0.4	L	∞	∞	15	110	128	512	0.01	80	322	5.2	0.4	0.8
J6[1]	50	0.4	$e^{-y'}$	∞	∞	35	110	128	256	0.02	90	1035	16.9	1.3	3.8
J7[1]	50	0.4	$e^{-3y'}$	∞	∞	35	110	128	256	0.02	90	1035	18.4	1.8	8.1
J8	25	0.4	L	500	1000	35	110	128	256	0.05	80	1840	29.0	2.9	4.6
J9	25	0.4	L	100	∞	35	110	128	256	0.10	80	1840	28.6	3.9	4.6
B1	25	0.2[2]	L	∞	∞	15	50	64	64	0.10	80	1840	14.8	2.5	5.0
B2	25	0.2[2]	L	500	2000	15	50	64	64	0.03	80	1840	14.0	3.2	5.0
B3	25	0.1[2]	L	500	2000	15	50	64	64	0.03	160	3681	13.6	3.5	5.0
D1	25[3]	0.2[2]	L	∞	∞	15	50	64	64	0.03	160	3681	13.7	3.9	5.1

TABLE 2—*Continued*

Case	min, max ν' (km^2 s^{-1})	min, max $\bar{\nu}$ (km^2 s^{-1})	min, max Δt (10^3 s)	Total time (days)	Time steps (10^3)	ΔT (K)	Final U_1 (m s^{-1})	Final $\hat{u}_{max}$ (m s^{-1})
J1	0.10, 0.30	0.01, 0.12	1.2, 5	2355	100	55.4	60.0	6.0
J2	0.05, 0.30	0.05, 0.3	1.5, 4	1480	64	91.3	104.0	14.0
J3	0.01, 0.06	0.01, 0.06	2.5, 4	873	28	27.9	29.8	3.3
J4	0.01, 0.04	0.01, 0.04	2, 4	402	14	15.7	27.6	3.0
J5	0.01, 0.03	0.01, 0.03	1, 4	353	16	10.0	38.7	3.4
J6[1]	0.04, 0.08	0.04, 0.08	2.5, 3	597	20	24.0	26.6	4.7
J7[1]	0.03, 0.15	0.03, 0.15	1.4, 3	318	20	18.4	36.1	4.5
J8	0.03, 0.15	0.03, 0.15	1.2, 4	1410	58	41.5	61.1	14.4
J9	0.10	0.10	1.7, 4	1527	60	42.9	37.2	12.2
B1	0.10, 0.15	0.01, 0.05	2.2, 5	3757	129	18.5	50.3	9.9
B2	0.10,	0.03	2.2, 3	4288	156	15.4	40.9	12.0
B3	0.10,	0.03	3	7306	220	13.2	28.2	7.5
D1	0.03	0.03	1.7, 3	1427	54	14.2	52.3	16.0

[1] Integration over active and nonactive regions.
[2] Equivalent to twice this value over full Y.
[3] Value at p_2 level, $\gamma_1^2=62$, $\gamma_3^2=16$ [s^2 km^{-2}].

The computational diffusion coefficient ν depends on resolution and is chosen empirically from test calculations—by examining spectral convergence and by keeping the turbulent Reynolds number R_T (see Part 1) near 2000.

e. Resolution

Four factors influence the choice of resolution and longitudinal sector size: an economic limit to 256×128 grid points, the need to have at least 16 grid points over the eddy scale L_ρ, the constraint that $X\geqslant4L_\rho$ for full nonlinearity (see Part 3), and the possibility of producing gyres of the size of the Great Red Spot. For the basic case J1 (Table 2) these conditions suggest a maximum sector size of 35 000 km, allowing an ample seven wavelengths across the domain. In cases where L_ρ is much smaller, the latitudinal resolution is increased to 512 grid points, while X is decreased to retain just seven wavelengths.

TABLE 3. Case J1: Instantaneous global means of energy and energy conversion. Units are 10^{-6} km^2 s^{-2} for K', $\bar{K}$, P'; 10^{-4} km^2 s^{-2} for $\bar{P}$; 10^{-12} km^2 s^{-3} for conversion terms; km^2 s^{-1} for diffusion coefficients; m s^{-1} for the rms velocity scale and K for ΔT. Time is measured from end of axisymmetric spinup.

Days	ΔT	U_1	K'	$\bar{K}$	P'	$\bar{P}$	$\{Q\bar{P}\}$	$\{\bar{P}P'\}$	$\{P'K'\}$	$\{K'\bar{K}\}$	$\{\bar{P}\bar{K}\}$	$\{\bar{K}F\}$	$\{K'F\}$	$\{\bar{P}F\}$	$\{P'F\}$	$\bar{\nu}$	ν'
0	29.4	2.3	0	5	0	168	211	0	0	0	0	0	0	0	0	0.01	0.10
43	30.2	3.3	3	5	2	176	216	13	8	0	0	0	1	0	1	0.01	0.10
58	30.4	8.1	36	10	18	178	218	99	78	16	3	0	13	0	5	0.01	0.10
104	30.1	17.6	176	61	59	182	221	101	75	12	3	0	31	0	9	0.01	0.10
178	30.6	22.7	201	241	45	192	226	49	54	80	5	1	23	0	6	0.01	0.10
247	31.3	25.1	140	425	36	203	232	36	36	23	7	3	16	1	5	0.03	0.10
316	32.3	25.1	94	488	12	216	240	−1	5	43	7	4	4	2	1	0.05	0.10
385	33.3	24.3	39	512	5	229	247	1	1	13	7	4	2	2	0	0.05	0.15
454	34.2	23.7	56	467	6	244	255	0	1	−4	7	3	2	2	0	0.05	0.15
522	35.3	23.1	34	465	5	258	262	1	1	3	8	3	1	3	0	0.05	0.15
591	36.3	22.6	40	438	5	274	270	1	1	−1	8	3	1	3	0	0.05	0.15
660	37.3	22.1	25	433	4	289	277	1	1	5	9	3	1	3	0	0.05	0.15
729	38.4	21.6	28	411	4	305	285	0	1	−1	9	3	1	3	0	0.05	0.15
798	39.4	21.2	24	398	4	322	293	2	1	3	9	3	1	3	0	0.05	0.15
867	40.4	20.8	18	388	3	339	300	2	1	−8	9	3	1	3	0	0.05	0.15
1004	42.5	20.1	20	359	5	374	315	4	1	−8	9	2	1	4	0	0.05	0.15
1142	44.5	19.6	17	342	5	410	330	5	2	3	10	2	1	4	0	0.05	0.15
1211	45.5	19.8	25	340	11	429	338	18	14	3	10	2	6	4	2	0.05	0.15
1279	45.9	25.4	13	453	52	444	344	193	139	−5	11	4	38	5	14	0.05	0.15
1306	45.5	29.4	258	510	81	448	345	234	142	−40	14	4	48	5	15	0.05	0.15
1392	45.2	49.6	888	1315	299	447	344	1247	885	1012	16	10	210	6	64	0.05	0.15
1443	44.9	67.9	1150	3100	242	428	337	1342	528	−1498	22	22	179	6	41	0.08	0.20
1471	43.6	73.7	948	4087	228	420	334	763	592	−10	3	44	188	10	55	0.08	0.20
1554	44.0	77.1	525	5135	115	422	334	218	187	408	17	65	85	11	24	0.10	0.25
1609	44.7	76.3	487	5077	105	429	337	216	111	−578	26	62	60	11	17	0.10	0.25
1671	45.5	74.4	269	5044	74	441	342	191	79	−395	2	74	42	13	14	0.12	0.30
1739	46.3	71.9	195	4782	54	457	348	30	20	−580	0	67	17	14	6	0.12	0.30
1773	46.8	70.6	187	4609	52	467	352	21	22	−112	4	62	16	14	6	0.12	0.30
1876	48.3	68.0	138	4352	44	491	361	25	24	593	5	56	18	14	6	0.12	0.30
1944	49.3	66.3	229	4028	55	510	368	28	63	−163	6	47	36	16	10	0.12	0.30
2013	50.3	65.2	83	4150	29	525	373	−65	16	48	8	26	17	15	8	0.12	0.30
2081	51.3	64.2	62	4042	22	546	380	39	8	−15	9	25	5	15	3	0.12	0.30
2150	52.3	63.2	64	3904	20	568	388	11	2	−15	1	23	3	16	1	0.12	0.30
2184	52.8	62.6	62	3837	22	579	392	4	2	−11	6	22	2	16	1	0.12	0.30
2355	55.4	60.0	45	3542	16	635	411	−1	2	5	5	20	2	17	1	0.12	0.30

f. Classes of solution

The solutions to be presented fall into five categories (Table 2). The main series (J1–J5) details the basic characteristics of quasi-geostrophic circulations and their dependence on the static stability. The second group (J6 and J7) examines the sensitivity of the circulations to the heating distribution $H_F(y)$. The effect of weak and strong surface drag on flow character is estimated for two cases (J8 and J9).

A trio of calculations (B1–B3) examines long-term flow equilibration with and without drag. To increase the efficiency of these lengthy calculations, the resolution and size of the β plane are reduced. The flow regime, however, remains comparable to that of the J cases. Another calculation with the smaller plane (D1) takes a preliminary look at the effects produced by a static stability that varies with height.

The calculations to be described are difficult to make, requiring high resolution and minimal dissipation, and the results depend partly on the computational factors. To proceed from such solutions to planetary application may require some extrapolation in parameter space.

4. The basic case: J1

The solution J1 exemplifies quasi-geostrophic circulations in the Jovian regime and is also optimal in computational accuracy and physical relevance.

The lengthy spinup of the J1 circulation begins with the baroclinic instability of the axisymmetric state and the generation of a multi-jet circulation. After a long quasi-steady phase, the multiple jets become baroclinically unstable, resulting in a flow with fewer but stronger jets. In the subsequent quasi-steady phase, the circulation takes on its equilibrated form. Contours of the most informative fields and integrals of the

energy conversion rates display the distinctive phases of this development (Figs. 4–15 and Table 3).[5,6]

a. First unstable phase: 0–316 days

The unstable axisymmetric state consists of a linearly varying temperature field with $\Delta T = 29.4$ K, together with a uniform zonal flow of ± 2.3 m s^{-1} in the upper and lower layers and a barely discernible Hadley cell (its maximum vertical velocity, 3×10^{-9} km s^{-1}, is close to the numerical round-off limit). Remnants of this state can be seen in the weakly perturbed fields of Fig. 4.

Although the waves form irregularly, the initial flow-development agrees with the predictions of linear theory in the scale selection (Fig. 3) and the correlation between variables (Fig. 4). The longitudinal wave scale corresponds to the radius of deformation ($k_x = 7$ in Fig. 3a) and the latitudinal scale to the length $(L_\rho L_{\bar{u}})^{\frac{1}{2}}$ ($k_y = 4$ in Fig. 3b), if $L_{\bar{u}} = Y$. As the instability amplifies, development becomes latitudinally localized and the scale $L_{\bar{u}}$ irrelevant (Fig. 5).

The axisymmetric flow form rapidly disappears as the nonlinear cascades create new distributions of zonal momentum. In areas where momentum formation is strong (e.g., the region marked A in Fig. 5a), the ζ and ψ' fields indicate the action of the β vortex-separation process, as described by Kuo (1951) and the solutions of Part 1. Eddies transfer westerly momentum and heat from the easterly to the westerly flows, so that the easterlies become more barotropic (Table 4). This separation of vorticity *and baroclinicity* suggests the existence of a partitioning process involving *potential vorticity*.

In keeping with the ideas of two-dimensional turbulence, the streamfunction eddies become larger in scale, and the potential vorticity and vorticity are more finely scaled into shear layers as the nonlinear cascades continue (Figs. 6a, 6b and 6f). Although a mean zonal flow exists, large gyres predominate—gyres whose convergence areas produce the quasi-geostrophic frontogenesis (Williams and Plotkin, 1968) apparent in Fig. 6e.

The generation of eddy kinetic energy (from potential) and the nonlinear cascading decline as wave propagation takes over in transferring the eddy kinetic energy into the mean zonal flow (Table 3). This transfer peaks at 178 days, by which time a proper jet-like circulation has begun to emerge (Fig. 7). Potential vorticity loses its fine layers and vertical motion becomes confined to the maximum baroclinicity areas of the westerly jets.

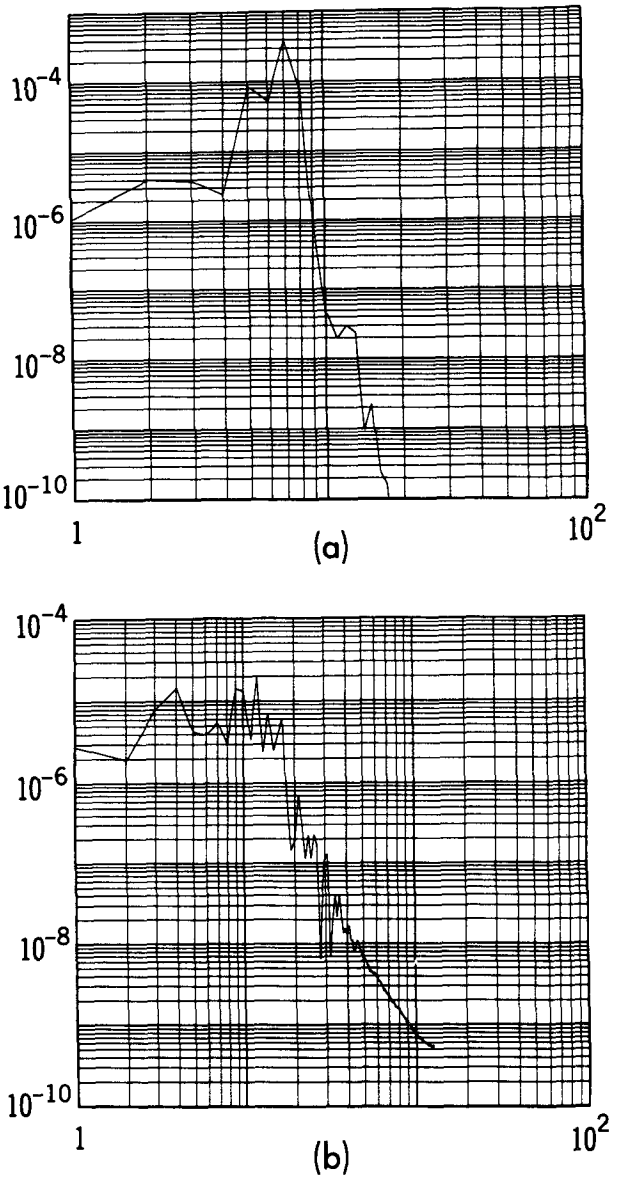

FIG. 3. Case J1 at 43 days: (a) longitudinal spectrum of u^2+v^2 at $y'=1/8$, (b) latitudinal spectrum of u^2 at $x'=\frac{1}{2}$. Abscissa is wavenumber.

The near-vanishing of the conversion integral $\{P'K'\}$ signifies the end of the first major instability at 316 days (Table 3). The velocity scale $U \approx 25$ m s^{-1} and the width of the five fully established jet pairs comply with the L_β relation, suggesting the action of the Rhines effect (Rhines, 1975) (Fig. 8). Less than 20% of the kinetic energy lies in the eddy mode and this proportion will decline to 3% over the next 900 days.

b. First quasi-steady phase: 316–1210 days

The flow now enters a quasi-steady phase in which the prevailing configuration at the end of the first major instability hardly alters for 3 years. However,

[5] Only *instantaneous* solutions are presented because the unpredictability of meaningful periods made time-averaging impractical. In some phases, energy conversions vary rapidly in sign, so the instantaneous values in Tables 3–5 reflect only the magnitudes of the terms and not overall tendencies.

[6] Note that parameter values associated with a number of these and subsequent figures require more space than is available in the legends. Complete legends are given in Appendix B.

weak energy conversions and momentum changes continue to occur as the ψ' contours (Fig. 9c) and the $\{K'\bar{K}\}$ integral testify.

Large-scale neutral baroclinic waves can be identified, in the quasi-steady phase, by a coincidence of the ψ' and $\hat{\psi}'$ contours in the presence of vertical shear (Figs. 9c and 10a). They have warm, high-pressure and cold, low-pressure correlations and form the interjet gyres. Their latitudinal and longitudinal length scales (L_β and X, respectively; see Fig. 1) indicate that these are forced waves driven by energy decascading, as in the Rhines effect.

Embedded within the neutral baroclinic waves in the maximum-baroclinicity area of the westerly jets are baroclinically unstable waves of scale L_ρ (in x and y). This form of instability occurs at a weaker baroclinicity than the major instability and transfers a small amount of heat locally (Table 3), thereby reducing the baroclinicity in the jet maxima (Fig. 9c profile) and retarding the onset of the major instability. Weak Ferrel cells form in association with these waves because of their steady, quasi-linear form (Fig. 9b profile).

At the end of the first quasi-steady phase (at 1140 days), five pairs of baroclinic westerlies and barotropic easterlies continue to coast along with minor adjustments being made through the propagation of neutral baroclinic waves (very much as in Fig. 9). During this phase, U has fallen from 25–19.6 m s^{-1} due to internal dissipation.

c. *Second unstable phase: 1200–1500 days*

The second major instability begins in the two most northerly jets and will eventually spread southward. As the eddy energy of the northerly instability cascades to a larger scale (Fig. 11c), frontogenesis occurs (Fig. 11e). The small-scale vertical motion (Fig. 11d) releases potential energy within the concentrated isotherms along which the local jet stream, boosted from 30–70 m s^{-1}, now flows. The northerly momentum gain remains localized and the other jets unaltered. The minor instability still occurs in the undisturbed jets but appears only in the zero contour values because of its relative weakness.

The instability of the central and equatorward zones sets in and peaks while that in the north decays (Fig. 12). Each zone remains unstable for ~200 days. At the end of the potential-energy release, the jets have attained 130 m s^{-1} maxima and have coalesced into four pairs to comply with the L_β scale (Fig. 13).

During the second instability phase, U increases from 19.6–77 m s^{-1}. This enormous gain indicates the strength of the instability and explains why the zonality of the quasi-steady flow was so drastically disrupted. In other solutions, where a strong zonal flow already exists, major instability phases do not cause a radical interruption of the circulation (see e.g., J9). This should also hold true during any further major instabilities in J1, for then $\bar{K} \gg K'$. However, the creation of powerful jets during the second instability requires that the time step be decreased from 3000 to 1200 s, precluding integrating as far as the third unstable phase *in this case.*

d. *Second quasi-steady phase: 1600–2400+ days*

As the calculation enters the second quasi-steady phase, the circulation consists of four westerly and two easterly jets (Fig. 14). A central easterly flow has been almost eliminated as the two central jets coalesce to meet the L_β constraint (cf. Figs. 14 and 15).

The dominant gyre, lying between the northernmost westerly and easterly flows, is permanent to the extent

TABLE 4. Case J1: Instantaneous momentum and temperature and their budgets at 58 days over the latitudes of jet formation (see Fig. 5a). Zonal velocity in m s^{-1} and its rate of change in units of 10^{-9} km s^{-2}. Temperature rate of change in units of 10^{-7} K s^{-1}.

j	$\bar{u}_1$	$-(\overline{u_1'v_1'})_y$	$f_0\bar{V}_1$	$\nu\bar{u}_{1yy}$	$\bar{T}_2$	$-(\overline{v_1'T_2'})_y$	HR^{-1}	$\overline{\tilde{\omega}_2}/\gamma^2 Rp_2$	$\nu\bar{T}_{2yy}$
152	0.69	−7.92	2.02	0.01	−3.03	−1.35	−0.17	0.18	0.01
154	0.33	−8.61	1.45	0.01	−3.02	1.26	−0.19	0.20	0.00
156	0.99	−3.74	1.34	0.01	−3.36	3.19	−0.20	−0.24	0.00
158	2.59	2.93	1.45	0.01	−3.54	0.73	−0.22	1.21	0.00
160	5.05	11.62	−2.66	0.02	−3.72	−1.55	−0.23	2.74	−0.01
162	8.34	25.53	−7.74	−0.03	−3.97	−1.28	−0.25	0.31	−0.01
164	9.16	18.77	−7.00	−0.06	−4.29	−0.30	−0.26	−2.22	0.00
166	6.16	−7.75	0.08	0.03	−4.58	8.64	−0.28	−5.49	−0.01
168	4.66	−3.33	9.83	−0.08	−4.96	−1.05	−0.29	1.40	0.02
170	−0.58	−0.07	3.95	−0.02	−5.23	−7.78	−0.31	3.39	0.03
172	−6.15	−7.67	−1.76	0.06	−5.31	−1.25	−0.32	−0.09	0.01
174	−7.38	−9.88	0.34	0.08	−5.33	5.06	−0.33	−2.75	−0.01
176	−3.35	−5.67	5.84	−0.01	−5.43	1.35	−0.35	−0.18	−0.02
178	0.45	−18.92	4.03	0.02	−5.68	−1.19	−0.36	2.09	0.00
180	5.19	4.24	0.79	−0.04	−5.95	3.62	−0.38	0.05	−0.01
182	7.29	10.39	0.15	−0.05	−6.30	−0.18	−0.39	0.85	0.01
184	5.91	10.09	−1.42	−0.01	−6.60	−0.57	−0.41	0.18	0.01
186	3.95	6.75	−1.70	0.00	−6.85	−0.96	−0.42	−0.04	0.01
188	2.16	−1.14	−1.29	0.01	−7.08	0.92	−0.44	−0.77	−0.01
190	1.42	−6.67	0.75	0.02	−7.31	2.98	−0.45	−0.88	0.00
192	1.54	−4.73	2.19	0.00	−7.57	2.77	−0.47	0.10	0.00

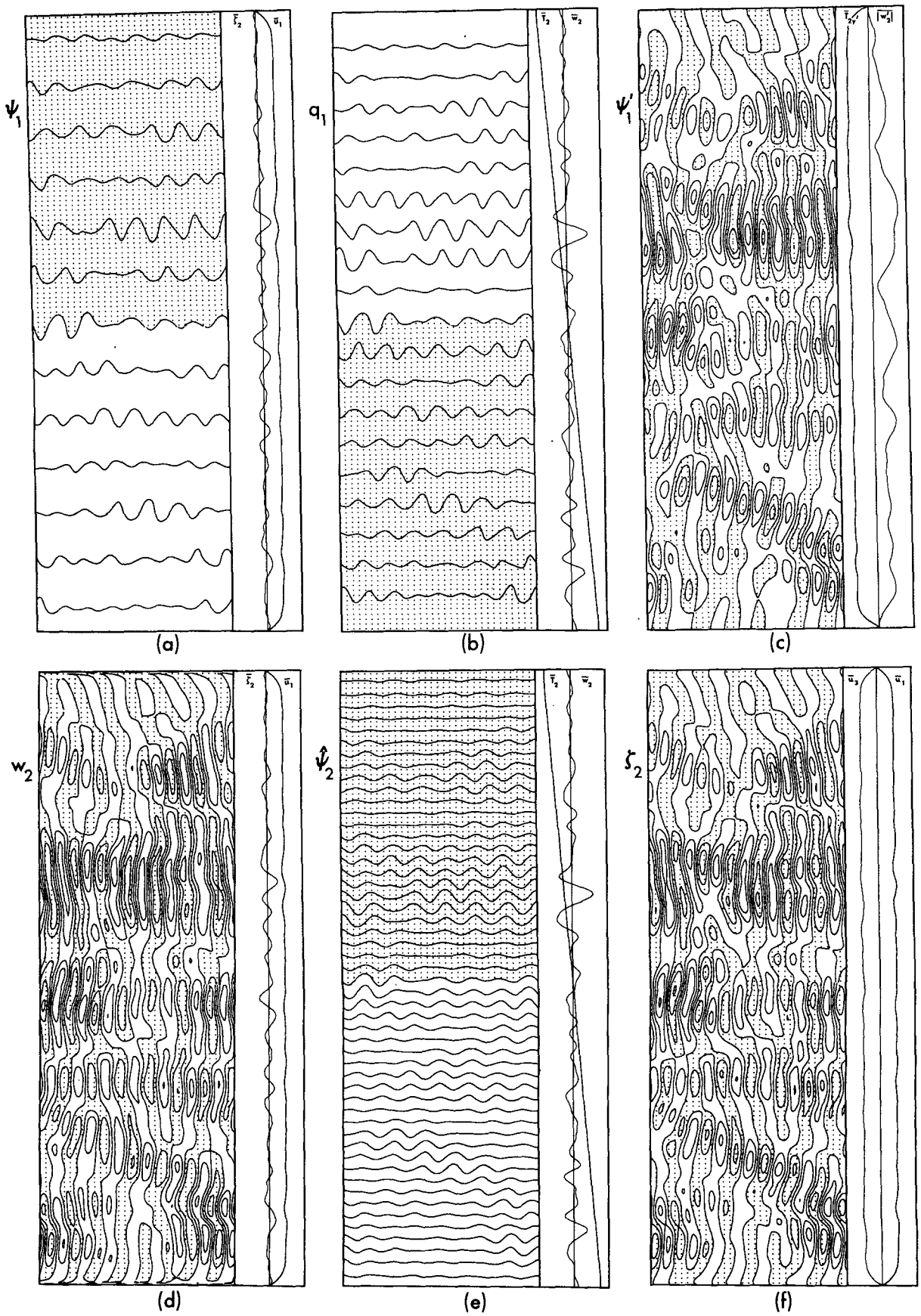

FIG. 4. Case J1 at 43 days. See Appendix B for further details.

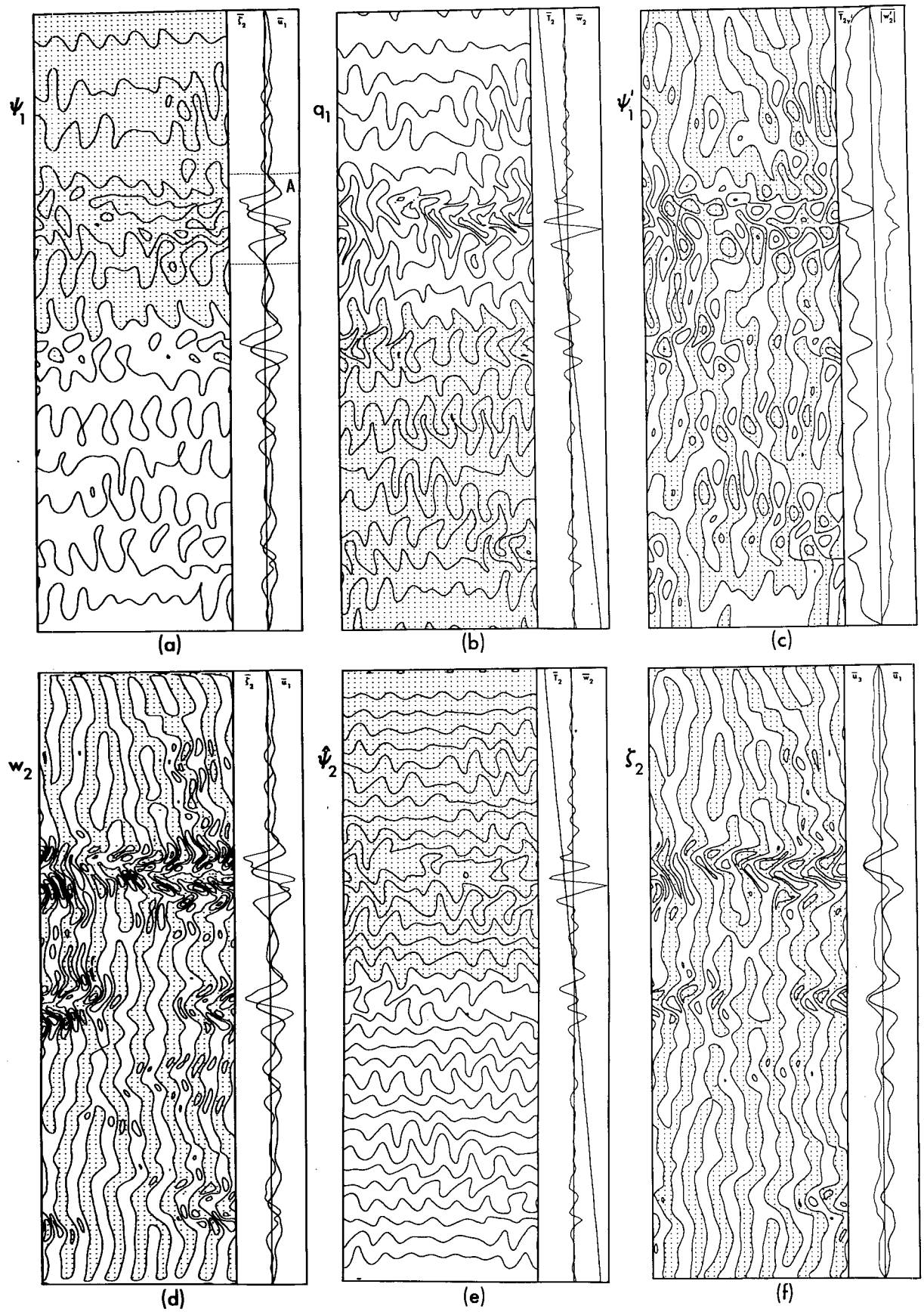

FIG. 5. Case J1 at 58 days. Variables and notation as in Fig. 4. A denotes jet formation area discussed in text.

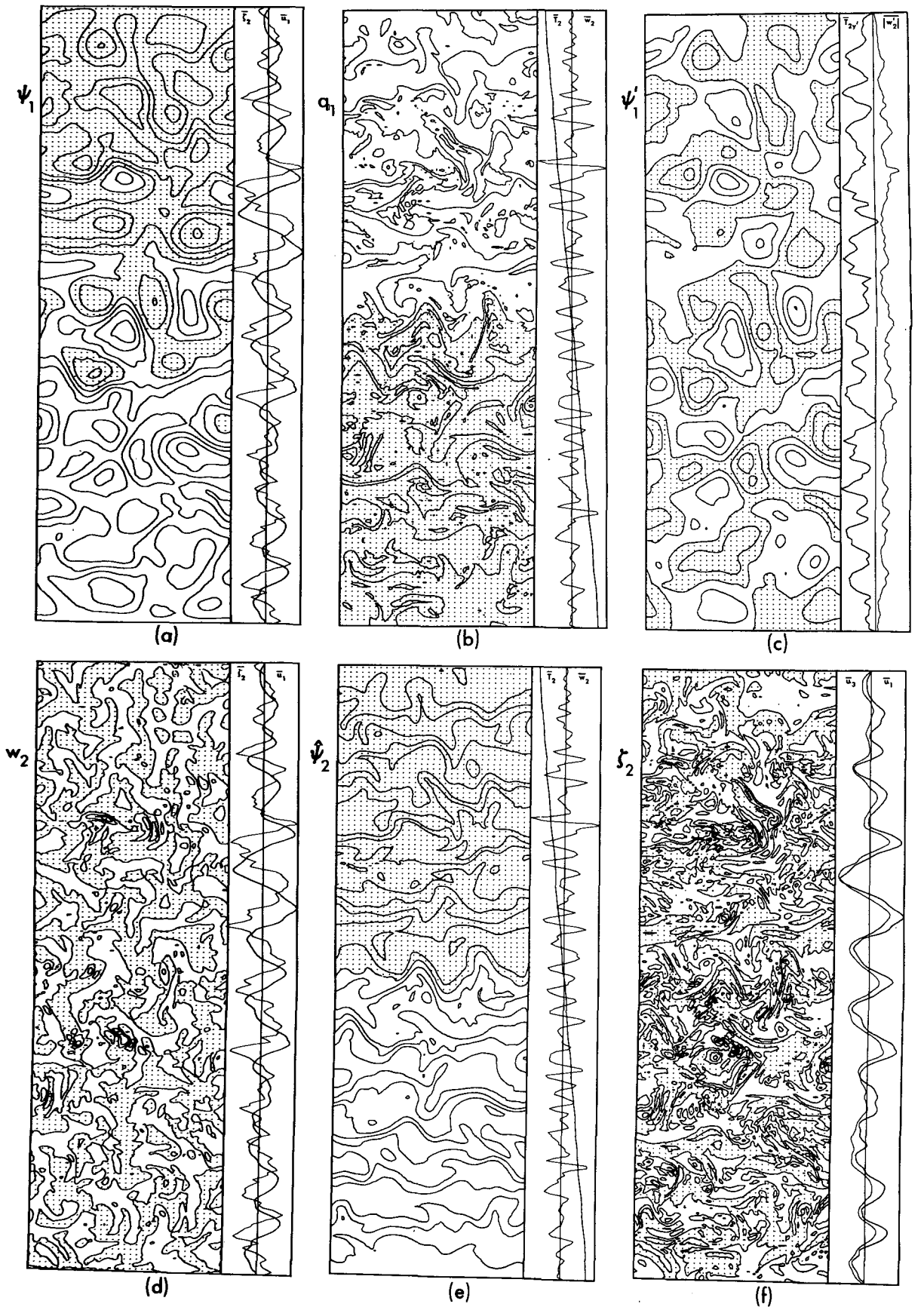

FIG. 6. Case J1 at 104 days, legend as in Fig. 4.

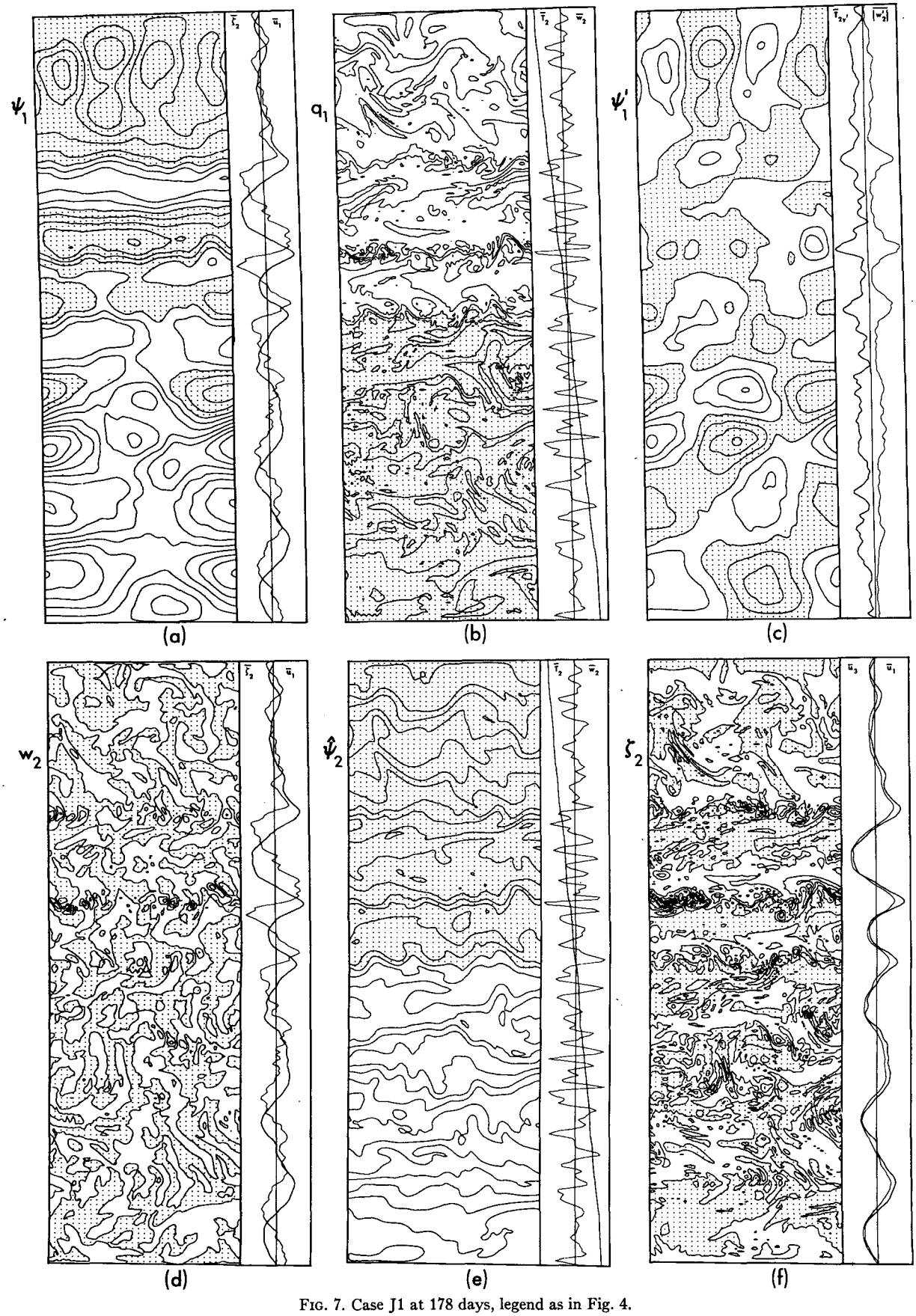

FIG. 7. Case J1 at 178 days, legend as in Fig. 4.

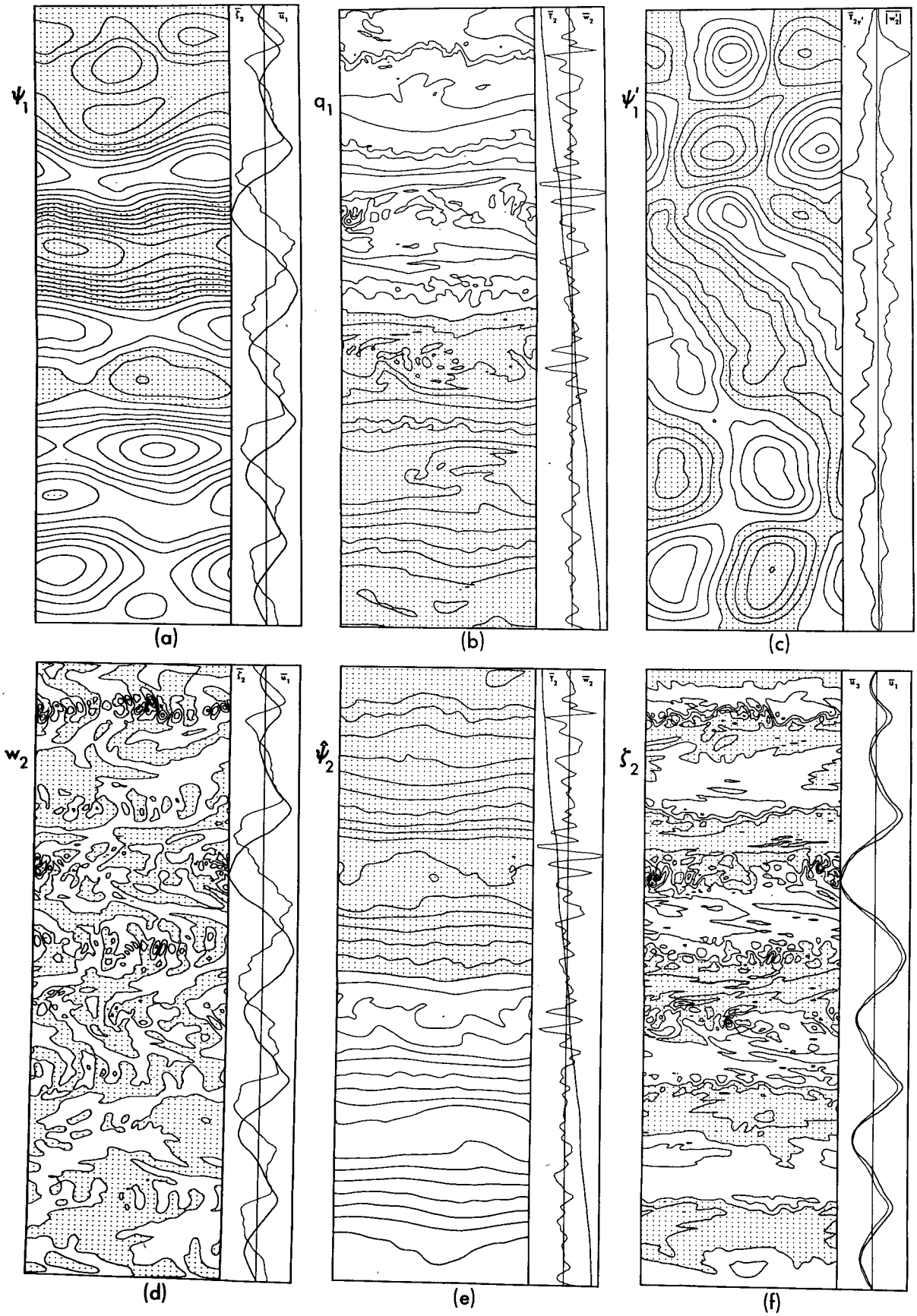

FIG. 8. Case J1 at 316 days, legend as in Fig. 4.

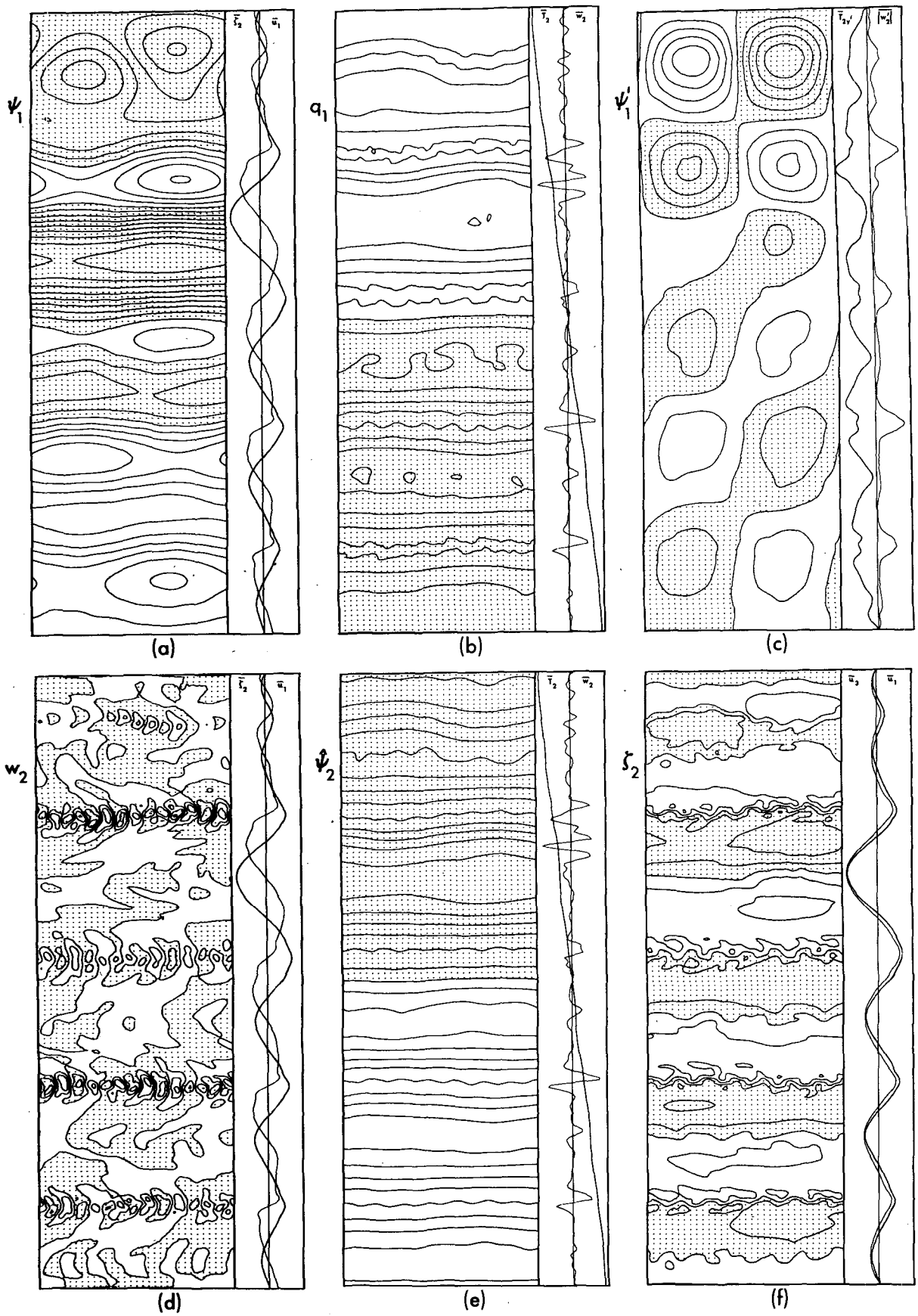

FIG. 9. Case J1 at 591 days, legend as in Fig. 4.

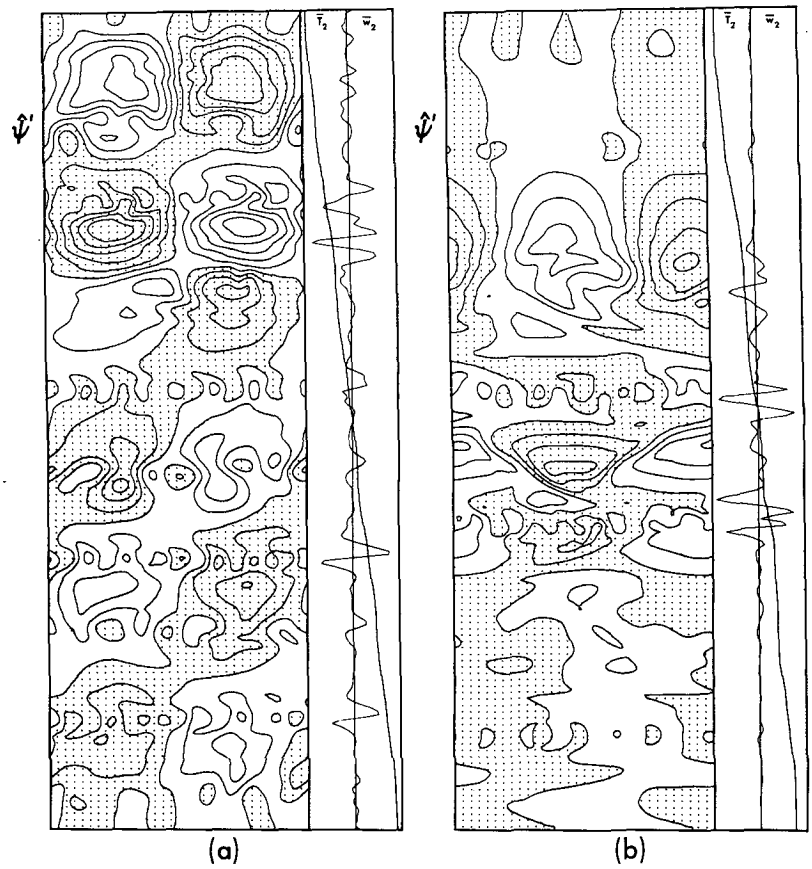

FIG. 10. Case J1 at (a) 591 days, (b) 1773 days. Perturbation temperature.

(a) $\Delta\hat{\psi}_2'=1.6$ km^2 s^{-1}, $T_2^*=20$ K, $w_2^*=5\times10^{-8}$ km s^{-1}
(b) $\Delta\hat{\psi}_2'=8.0$ km^2 s^{-1}, $T_2^*=30$ K, $w_2^*=7\times10^{-7}$ km s^{-1}.

that it exists continuously from its inception at 1400 days to the end of the calculation at 2355 days. For convenience, we will refer to it as the "Gyre." The $\hat{\psi}'$ and ψ' fields (Figs. 10b and 14c) indicate that the object is centered on the warm, high-pressure region of a neutral baroclinic wave. During the interval from 1773–1825 days, the Gyre moves eastward at an average speed of 0.5 m s^{-1} but, in general, motion can be in either direction.

The solution is terminated at 2355 days for economy and also because it is not equilibrating. An excessive heating rate causes the thermal imbalance: eddy heat transport can only reduce ΔT by 5 K per 10^3 days under a heating rate that produces a rise of 15 K per 10^3 days. Reducing H_a to a more appropriate rate of 0.15 units would result in formidable computational demands, by lengthening the integration period and exposing the circulation to greater computational dissipation during the quasi-steady phases. The equilibrated solutions of Section 8 suggest that a more realistic J1 circulation would vary about the above features, rather than continuing to evolve toward a state with a single strong jet.

e. J1 *and Jupiter's bands*

Turning to the planetary implication of the J1 solution, a detailed comparison of the model's dynamics with that of Jupiter's atmosphere would not be relevant and would be extending the analogy beyond its intended limit. It is of interest, however, to draw attention to those characteristics that are common to both systems.

Both circulations consist of multiple easterly and westerly jets with a strong zonal orientation and of latitudinal motions that are weak except near the inter-jet gyres. In the model, small-scale vertical motions of order 10^{-5} and 10^{-6} km s^{-1} occur in the major and minor baroclinic instabilities, but no large-scale mean vertical motions exist; the Jovian situation is unknown.

Extrapolating from J1 to more weakly-heated, equilibrating model flows suggests the existence of energy cycles with 3–7 year periods. Some cyclic behavior, with periods ranging from 3–8 years, can also be observed in band motions on Jupiter (Fig. 16), and appropriately attributed to inertial effects. Northward band movement occupies less than one-third of each cycle, as does the major instability phase in the model circulations.

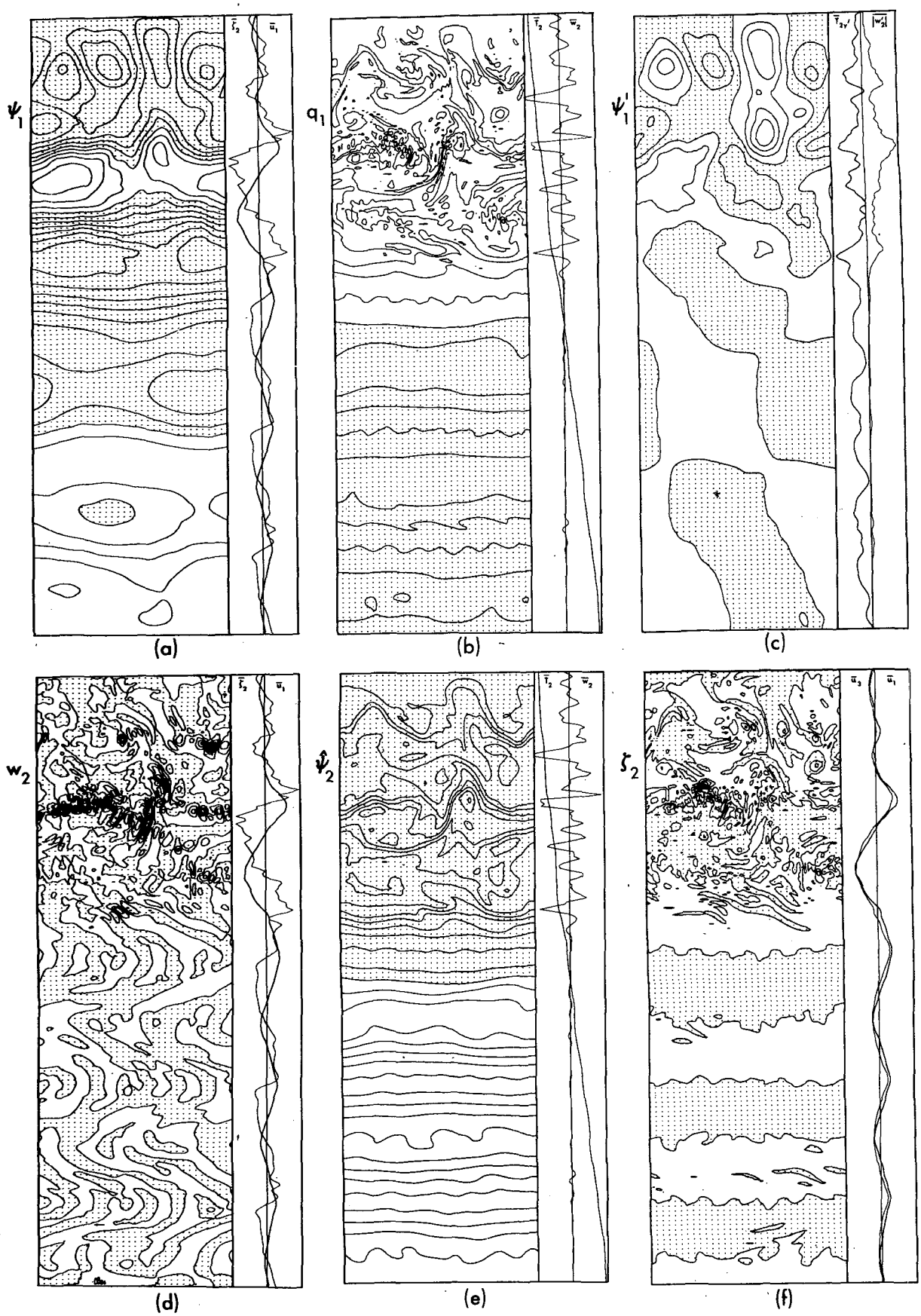

FIG. 11. Case J1 at 1306 days, legend as in Fig. 4.

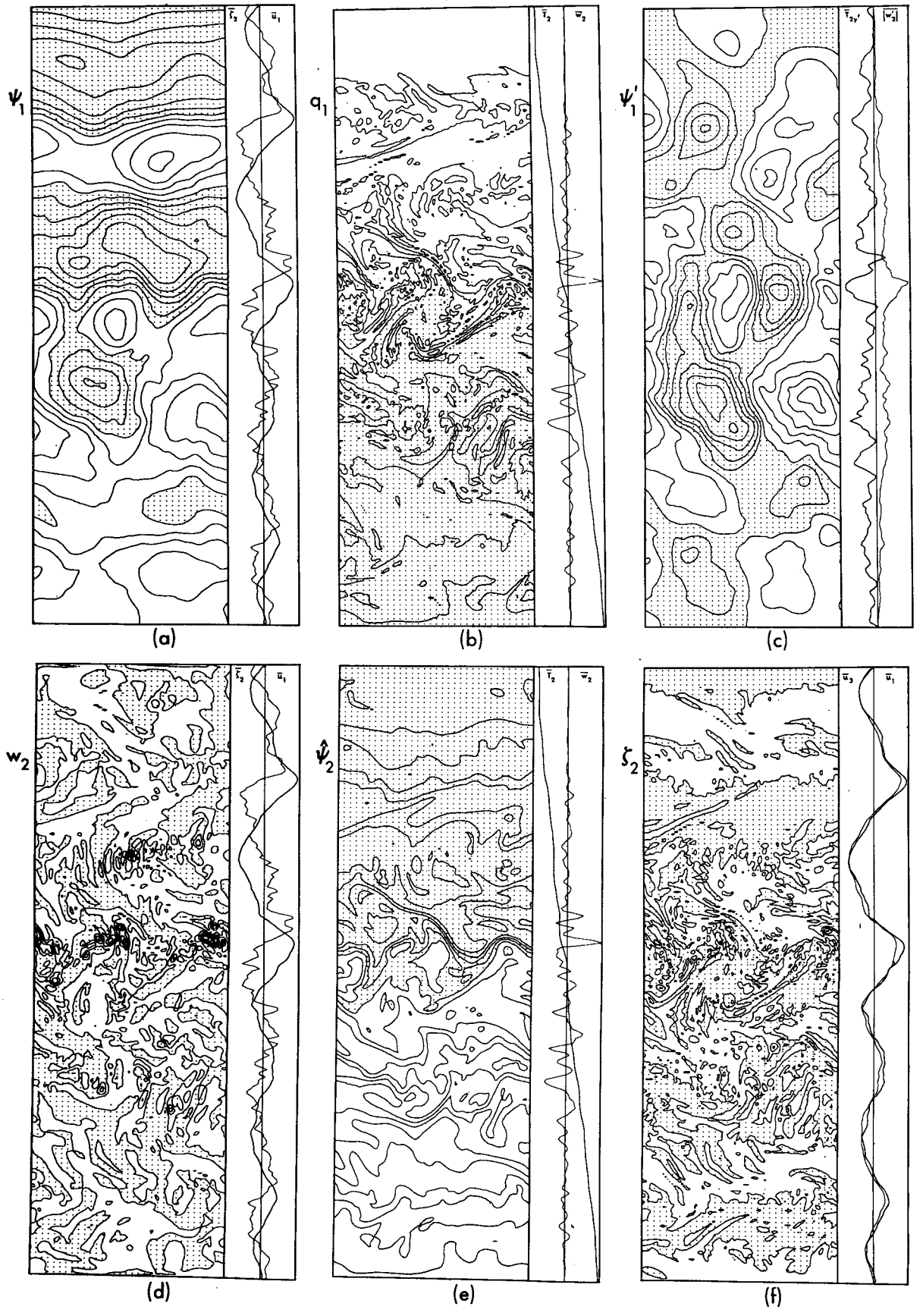

FIG. 12. Case J1 at 1392 days, legend as in Fig. 4.

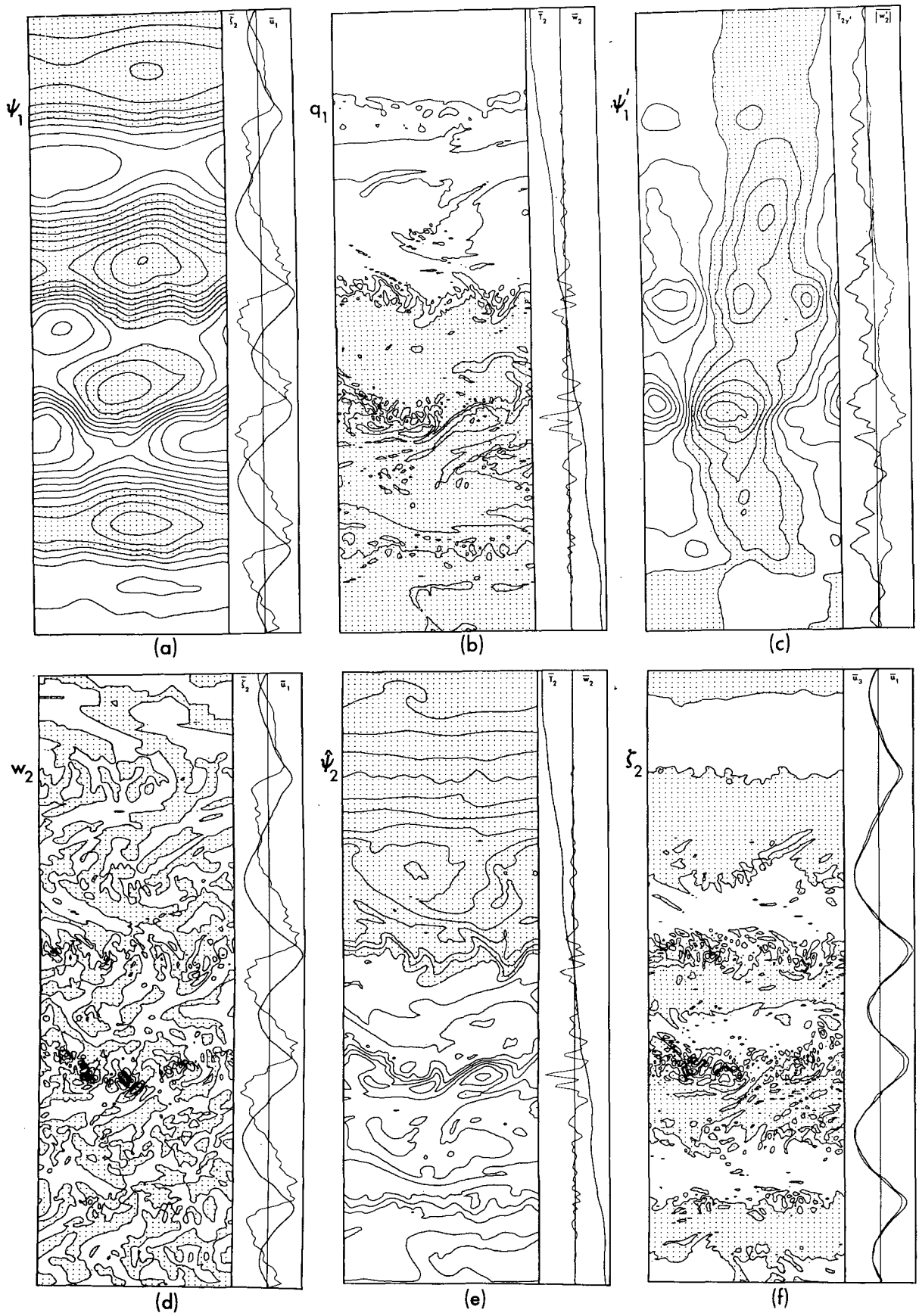

FIG. 13. Case J1 at 1471 days, legend as in Fig. 4.

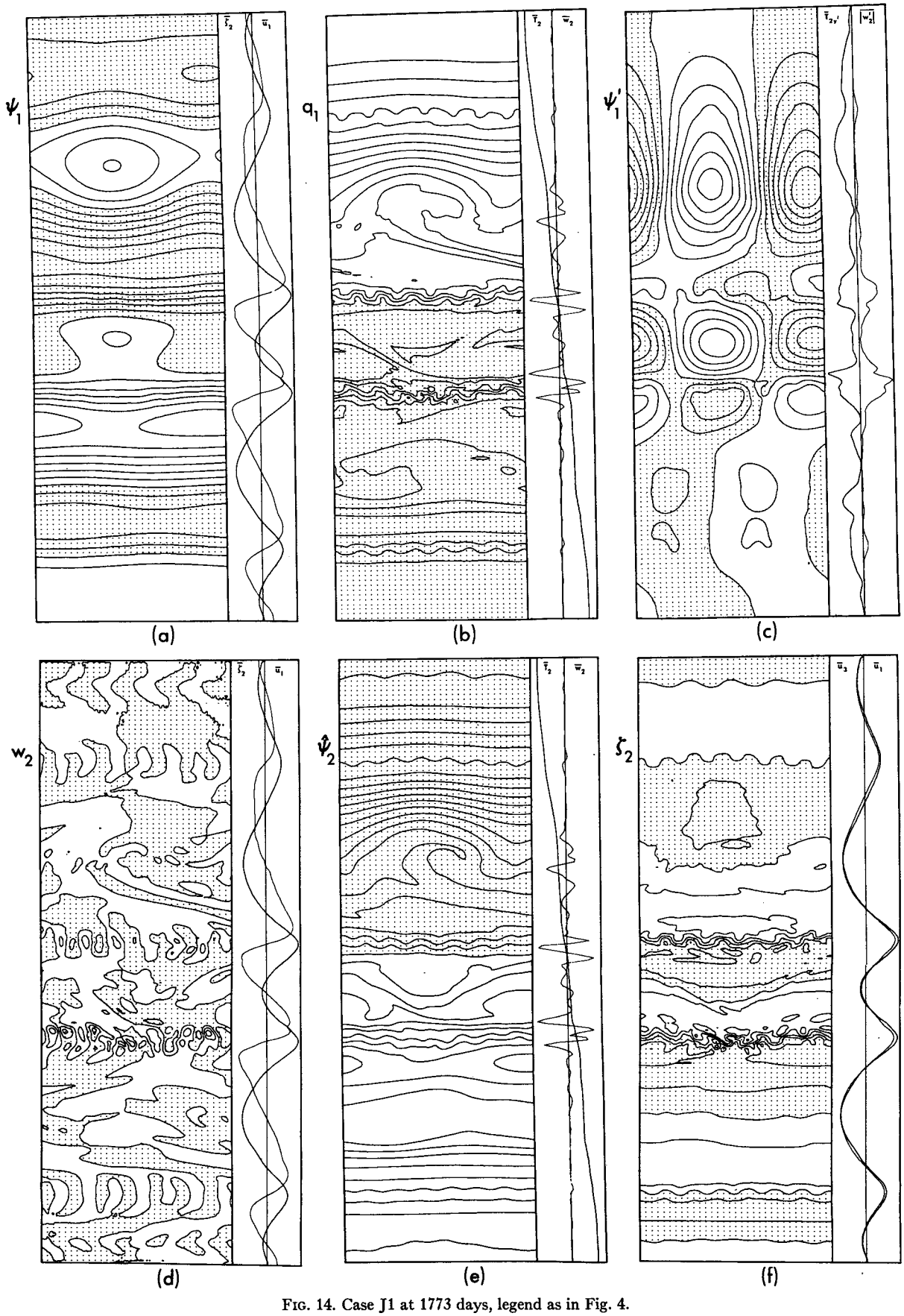

FIG. 14. Case J1 at 1773 days, legend as in Fig. 4.

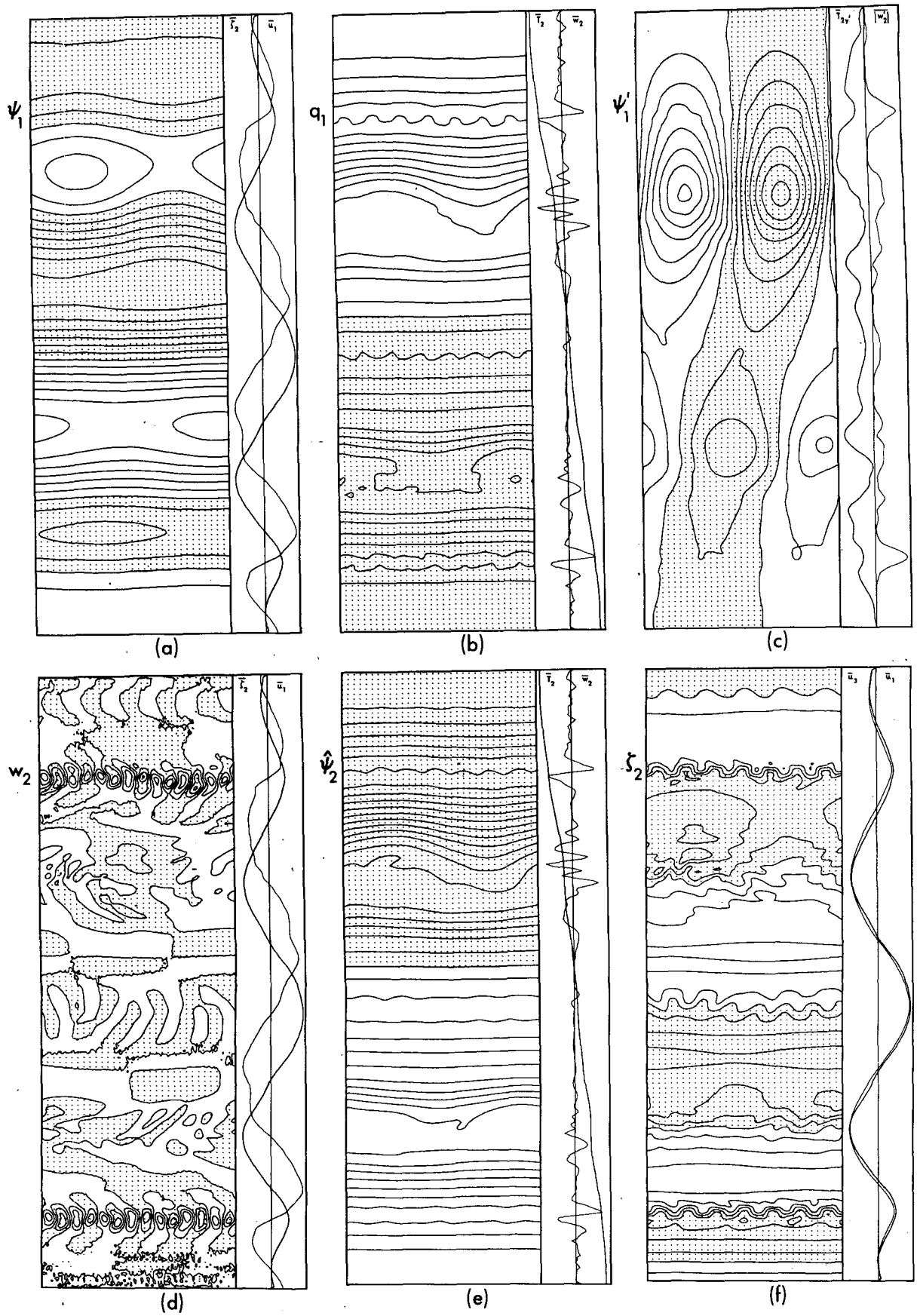

FIG. 15. Case J1 at 2184 days, legend as in Fig. 4.

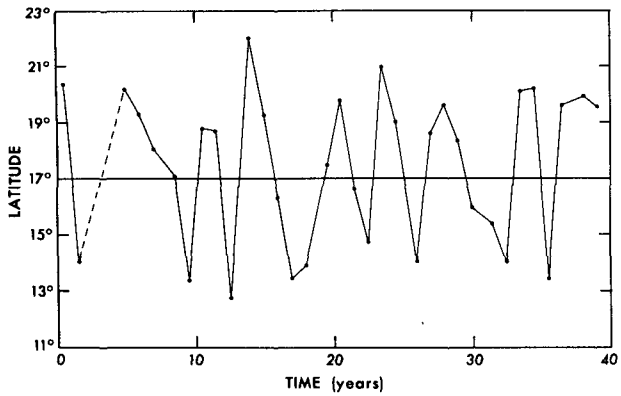

FIG. 16. Latitudinal position of the northern edge of North Equatorial Belt of Jupiter as a function of time, beginning in 1908 (after Peek, 1958). Dotted line interpolates data.

f. J1 *and the Great Red Spot*

The Gyre and Great Red Spot are both warm, high-pressure anomalies and possess many features in common: an anticyclonic zonal-mean flow environment and the same latitudinally anisotropic distribution of adjacent eddies, a latitudinal uniqueness and a slow longitudinal drift (in either direction), a quasi-permanence and a shape that varies from elliptical at the boundary to oval at the core [cf. Fig. 15a and Gehrels' (1976, Fig. 8)]. The Gyre corresponds to just the central part—"the tip of the iceberg"—of a forced, neutral baroclinic wave with a latitudinal scale of L_β; neither the cause of the Great Red Spot nor its extent beyond the visible portion are known.

The two objects differ mainly in their *longitudinal* uniqueness and scale. However, because the above similarities imply that the Great Red Spot can be described by the quasi-geostrophic equations [i.e., ageostrophic effects (hurricanes, topography, etc.)[7] are superfluous], differences in scale selection must be due to the *two-layer approximation* to the equations. Both objects lie well within the ultralong wave regime discovered by Green (1960). The normal mode characteristics of this regime require a minimum of four layers for their proper representation (Hirota, 1968) and, for the parameters of the Jovian regime, the preferred ultralong waves occur at length scales two to three times larger than for Earth (Fig. 17) [see Williams (1979)].

In the four-level model, gyres could be produced in association with the ultralong baroclinically unstable waves, rather than with the neutral waves, but would be similar to the Gyre because of the quasi-neutral form of the instability. In addition, such gyres could be self-sustaining (in a weakly dissipative atmosphere) because of their small energy supply. The preferred wave scales are 34 000, 24 000 and 17 000 km when $\gamma^2=5$, 10 and 25 s^2 km^{-2} and $\hat{u}=40$, 20 and 10 m s^{-1}, respectively. The Great Red Spot is presently 28 000 km by 14 000 km in size.

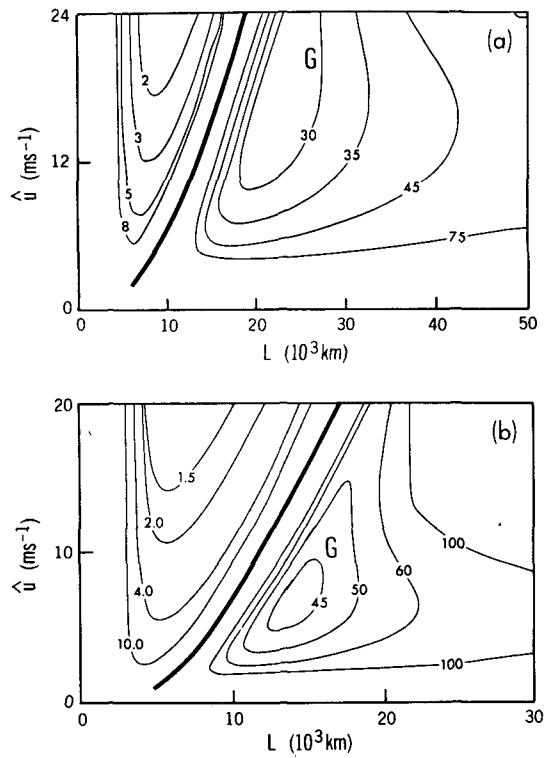

FIG. 17. Baroclinic instability growth rates of Jovian regime with doubling time in days for four-layer model (after Hirota, 1968). G denotes preferred scale of gyres: (a) $\gamma^2=10$ s^2 km^{-2}, (b) $\gamma^2=25$ s^2 km^{-2}.

Analysis of the Gyre in terms of normal-mode concepts cannot account for the longitudinal uniqueness of the Great Red Spot. A similar difficulty occurs in understanding localized cyclogensis in the Earth's atmosphere. Spatial instabilities (Thacker, 1976; Merkine, 1977) can explain localized activity for localized sources but not for homogeneous sources such as occur in the Jovian situation.[8] Pending current investigations, we conjecture that an analogy exists (within the limitations of normal-mode concepts) between the Great Red Spot and an optimally selected, ultralong, near-neutral, localized baroclinically unstable wave. In short, the Red Spot could be a Green wave.

g. J1 *and Jupiter's cloud formation*

The similarity between the streamfunction—rather than the temperature, vertical motion or vorticity[9]—of the Gyre and the clouds of the Great Red Spot

[7] Semi-permanent high pressure areas, such as the Aleutian stratospheric anticyclone, may provide the only (limited) terrestrial analogy to the Great Red Spot (cf. Mahlman and Moxim, 1978, Fig. 4.2).

[8] In Part 3, we show that localized cyclogenesis can occur in the homogeneous case, particularly when Thacker's criterion $\tilde{U}>2\frac{1}{2}\hat{U}$ is met—a condition highly favored in the Jovian regime.

[9] This distinction cannot be made for the jets and bands and this led us to suggest in Part 1 that vertical circulation cells induced by Ekman pumping could cause the clouds. The less-ambiguous structure of the (baroclinic) Gyre eliminates this possibility.

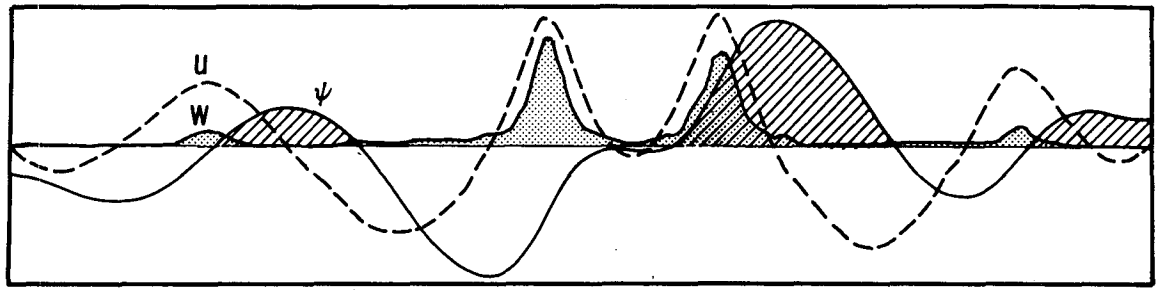

FIG. 18. Latitudinal profiles of $\bar{\psi}_1$, $|\overline{w_2'}|$, $\bar{u}_1$ at 1825 days; pole on the left, equator on the right. Lined shading corresponds to clouds of zones ($\psi_1 > 0$), dotted shading to eddy clouds. $\psi_1^* = 1000$ km^2 s^{-1}, $|w_2'|^* = 2 \times 10^{-5}$ km s^{-1}, $u_1^* = 160$ m s^{-1}.

suggests that the larger scale Jovian clouds may be correlated with horizontal variations in the pressure deviation.[10] Such mechanically induced clouds would resemble the terrestrial cirrostratus forms, such as sometimes occur, appropriately enough, on the equatorward side of the jet stream.

If Jupiter's cloudy Zones correspond to the high pressure areas ($\psi > 0$) of the model, then the observed differential rotation of those bands reflects directly the geostrophic balance $u = -\psi_y$ (Fig. 18) and not (indirectly) the vertical motion associated with convective models of cloud formation. This would be in agreement with the quasi-geostrophic view that the circulation is essentially horizontal.

The separation in scale between the variations in the geostrophic-pressure and the w, T fields is greater in the Jovian regime than the terrestrial. This allows clouds to form in close association with both sets of variation as shown in Fig. 18: the smaller eddy clouds (represented by $|w'|$ profile) being mainly visible within the larger banded clouds (represented by the ψ profile) where the amplitude of the pressure variations is weakest. The existence of eddy clouds on just the poleward edges of the Jovian Zones supports this view.

5. Static-stability variation: J2–J5

The parametric dependence of the circulations is evaluated for four wide-ranging values of the static-stability (Table 2). Surface drag is omitted in all cases. Table 5 documents the energy budget at the end of each calculation.

a. J2: $\gamma^2 = 10$ s^2 km^{-2}

Zonal jets form rapidly (in 150 days) in this strongly stable fluid and by 299 days have evolved into four westerly jets of 130 m s^{-1} magnitude (Figs. 19a and 19b).[11] The first quasi-steady phase sets in at 450 days with a velocity scale of $U_1 = 76$ m s^{-1} and at 500 days the three northernmost jets merge into a single 150 m s^{-1} flow. This jet increases to 230 m s^{-1} during the second major instability, which begins at 1200 days (Figs. 19c and 19d). The large northerly gyre, corresponding to the cold low-pressure area of a neutral baroclinic wave, is transient.

With its broader bands, stronger flow and larger baroclinicity, the J2 solution may be more relevant to Saturn than Jupiter. [A solution with the same parameter values as J2, but using the Phillips' system of boundary conditions, was discussed in Williams (1975)].

b. J3–J5: $\gamma^2 = 50$, 100, 250 s^2 km^{-2}

Although the potential energy is released more slowly and at smaller scales in the low vertical-stability cases, strong zonal circulations develop if high-resolution and low- (perhaps marginal) diffusion coefficients are used.

Initial flow development parallels that of J1 and by the first quasi-steady phase four to six pairs of jets, with magnitudes ranging from 50–80 m s^{-1}, have evolved through the decascade (Fig. 20). Surprisingly, the flow with the weakest static stability and baroclinicity (J5) is the strongest. Again gyres of sector size form. The smaller eddies transfer less heat, suggesting that heating rates less than 0.1 units are necessary for equilibration in these cases (Table 2).

The basic similarity of the large-scale circulation patterns in J1–J5 indicates the unimportance of eddy size or baroclinicity level—they range from 2000–9500 km and 5–90 K—in forming what are essentially quasi-barotropic features. This universality justifies parametric extrapolation in drawing analogies with the planetary flows.

6. Baroclinicity variation: J6, J7

Although the above solutions indicate that flow-form does not depend crucially on static stability, a circulation can be modified by *latitudinal variations* in the static stability, the β term and the heating gradient $\partial H_F/\partial y$. To examine the last of these effects, two simple exponential heating functions are used (Fig. 2)

[10] The deviation is from some standard atmospheric pressure that is a function of height only.

[11] Even in the most complex flow stages of J1, the larger and smaller scales of the q distribution reflect the T and w fields. This conciseness justifies plotting only the ψ, q variables to represent the other solutions.

TABLE 5. Instantaneous energy conversion and other integral mean values at the end of each calculation. Units are 10^{-6} km^2 s^{-2} for K', $\bar{K}$, P'; 10^{-4} km^2 s^{-2} for $\bar{P}$; 10^{-12} km^2 s^{-3} for conversion terms; m s^{-1} for the rms velocity; K for ΔT; km^2 s^{-1} for $\bar{\psi}_L$. Time is measured from end of axisymmetric spinup.

Case	Days	ΔT	$\bar{\psi}_L$	U_1	K'	$\bar{K}$	P'	$\bar{P}$	$\{Q\bar{P}\}$	$\{\bar{P}P'\}$	$\{P'K'\}$	$\{K'\bar{K}\}$
J2	1480	91.3	0	103.7	684	9731	78	725	692	50	23	−586
J3	873	27.9	0	29.8	186	671	27	329	419	13	3	−83
J4	402	15.7	0	27.6	112	624	24	201	462	23	9	−35
J5	354	10.0	0	38.7	274	1182	73	191	713	90	127	−100
J6	597	24.0	0	26.6	49	630	8	239	358	6	3	−10
J7	318	18.4	0	36.1	354	907	32	161	301	−23	3	377
J8	1410	41.5	−357	61.1	109	3502	13	388	321	35	6	−141
J9	1527	42.9	−642	37.2	307	945	109	379	317	353	232	32
B1	3757	18.6	0	50.3	65	2357	22	72	69	116	82	173
B2	4288	15.4	−380	40.9	57	1509	16	46	55	24	31	16
B3	7306	13.2	−216	28.2	34	706	13	40	26	34	32	43

TABLE 5—(*Continued*)

Case	$\{\bar{P}\bar{K}\}$	$\{\bar{K}F\}$	$\{K'F\}$	$\{\bar{K}D\}$	$\{K'D\}$	$\{\bar{K}I\}$	$\{K'I\}$	$\{\bar{P}F\}$	$\{P'F\}$	ν'	$\bar{\nu}$
J2	8	80	19	—	—	—	—	48	4	0.30	0.30
J3	1	4	2	—	—	—	—	4	1	0.06	0.06
J4	0	4	4	—	—	—	—	2	2	0.04	0.04
J5	2	8	51	—	—	—	—	2	20	0.03	0.03
J6	0	8	2	—	—	—	—	5	1	0.08	0.08
J7	−1	10	6	—	—	—	—	5	1	0.15	0.15
J8	4	40	5	34	1	1	0	13	1	0.15	0.15
J9	0	12	61	44	12	—	—	9	15	0.10	0.10
B1	2	22	36	—	—	—	—	5	11	0.15	0.15
B2	−2	10	23	14	0	0	0	2	6	0.10	0.03
B3	−1	4	14	6	0	0	0	1	3	0.10	0.03

for a fluid with a moderate stability ($\gamma^2 = 50$ s^2 km^{-2}) and a drag-free surface (Tables 2 and 5).

a. J6: *Moderate baroclinicity variation*

In the moderately exponential heating function, the gradient at the poleward end is only one-third that at the equatorial boundary, in keeping with the possibility that the polar regions of Jupiter are uniformly heated by the interior source. As a result of this uneven baroclinicity, instability sets in earlier and more strongly and produces jets in the equatorial third of the β-plane (Figs. 21a and 21b). By the first quasi-steady phase, a weaker zonal flow has also developed in the central region (Figs. 21c and 21d).

b. J7: *Strong baroclinicity variation*

Heating with the strongly varying function—the baroclinicity is 20 times greater at the equatorial end—leads to the simultaneous and rapid development of a predominating westerly jet and anticyclonic gyre, (Figs 21e and 21f). As in J6, the localized flows are stable and the zonal momentum remains in the region of production.

An additional analogy exists between the J6, J7 solutions and Jupiter, in that both have stronger jets near the equator and none beyond 50 ° latitude (see Fig. 1, Part 1). Whether the planetary characteristics are also caused by baroclinicity variations, rather than by β, γ^2 variations, is unknown.

7. Drag variation: J8, J9

To illustrate the effect of surface drag on quasi-geostrophic circulations, we present two cases: one typical of weak drag, the other of strong drag. Both correspond to a reevaluation of J1 with the τ_D, τ_I terms activated and with diffusion simplified by setting $\bar{\nu} = \nu'$.

a. J8: *Weak drag*

When $\tau_D \approx 500$ days, the drag only influences the circulation moderately, in that momentum equilibrates without altering the character of the flow (Figs. 22a and 22b). In the second quasi-steady phase, the circulation J8 reveals a basic similarity with J1, despite differences in the number and the amplitude of the jets and in the incidence of the major instability—the first instability ends at 450 days (300 days in J1) and the second one starts at 1000 days (1200 days in J1) in the equatorward area (poleward area in J1). Any vertical motion due to Ekman pumping would be of order 10^{-6} km s^{-1} for the J8 parameters.

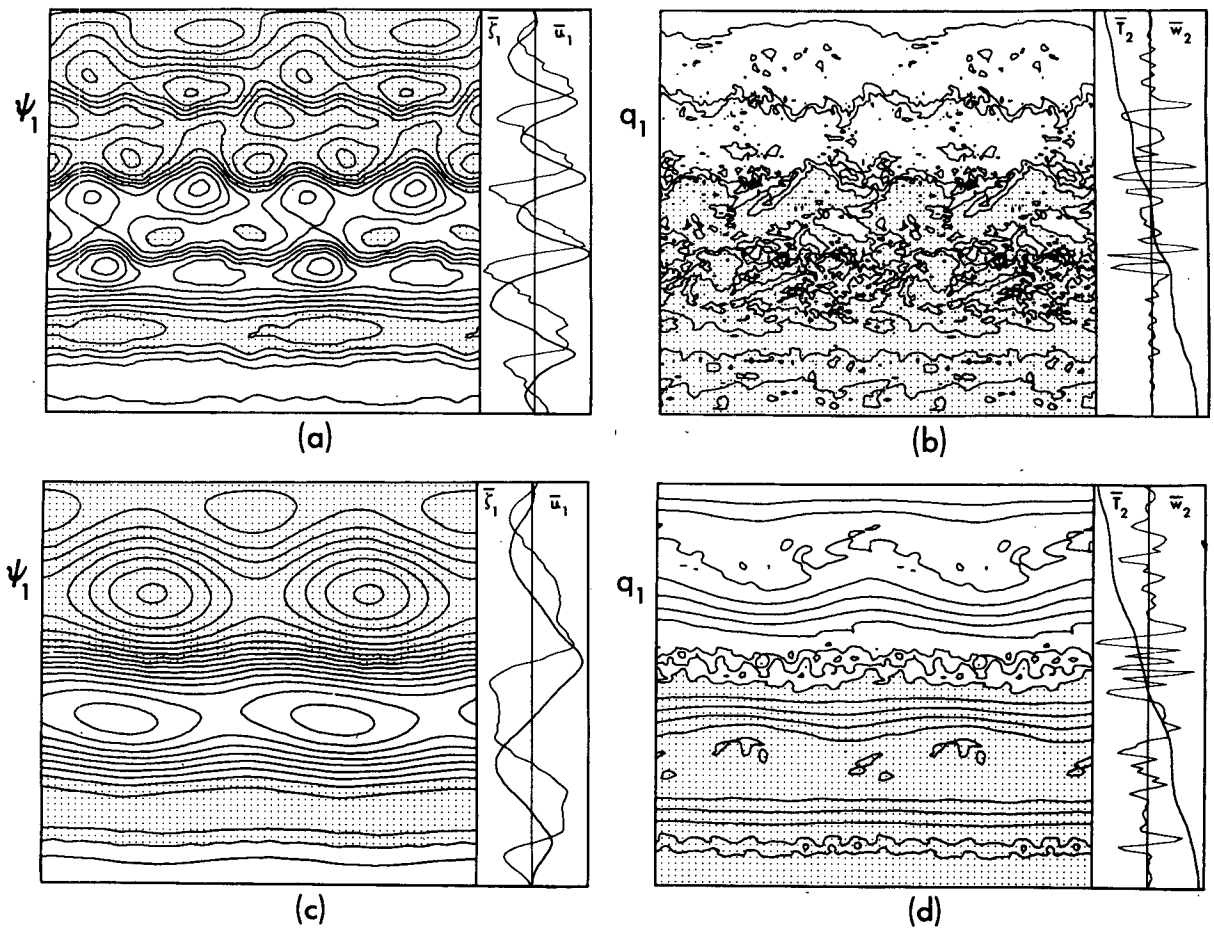

FIG. 19. Case J2 at 299 days (a,b) and 1480 days (c,d). Basic fields and profiles are ψ_1, $\bar{u}_1$, $\bar{\zeta}_1$ on the left and q_1, $\bar{T}_2$, $\bar{w}_2$ on the right. Integration sectors are repeated r times longitudinally to yield an optimum plotting area approximately equivalent to the quadrant of a sphere. Other notation as in Fig. 4. $r=2$ in all frames.

(a) $\Delta\psi_1=150$ km^2 s^{-1},	$u_1^*=120$ m s^{-1},	$\zeta_2^*=3\times10^{-5}$ s^{-1}
(b) $\Delta q_1=8\times10^{-5}$ s^{-1},	$T_2^*=40$ K,	$w_2^*=2\times10^{-6}$ km s^{-1}
(c) $\Delta\psi_1=300$ km^2 s^{-1},	$u_1^*=250$ m s^{-1},	$\zeta_2^*=2.5\times10^{-5}$ s^{-1}
(d) $\Delta q_1=5\times10^{-5}$ s^{-1},	$T_2^*=50$ K,	$w_2^*=2\times10^{-7}$ km s^{-1}.

b. J9: *Strong drag*

When $\tau_D\approx100$ days, the surface drag significantly modifies both the character and energy cycle of the circulation. The quasi-steady phases are shorter and the first three major instabilities of J9 occur between days 0–200, 500–770 and 1050–1210. At the end of the third quasi-steady phase (at 1500 days) U_1 has decayed to 34 m s^{-1}, indicating a rapid momentum equilibration under this strong drag. However, the mean baroclinicity ΔT increases continuously from 28.6–42.9 K (Tables 2 and 5), implying the need again for a reduced heating rate.

The lack of disruption of jet zonality during the third major instability of J9 (Figs. 22c and 22d) contrasts with the second instability of J1 and illustrates the stability of fully developed jets. However, because of cascade blocking by the strong drag, the flow is basically less zonal than that of J1—this is most apparent in the third quasi-steady phase (Figs. 22e and 22f). To balance momentum loss at the surface the westerlies are stronger and more concentrated than the broader easterlies. As a consequence of this asymmetry the gyres are less elliptical in shape than those of J1.[12]

Comparing J1, J8 and J9 with Jupiter leads to the conclusion that drag on the planet must be weak ($\tau_D\gtrsim500$ days), if the quasi-geostrophic model is relevant. The interface stress, represented by the τ_I term, also appears to be weak, but its indistinctive role makes it difficult to isolate quantitatively.

[12] Terrestrial analogs to the Great Red Spot, if they exist, will also be non-elliptical for the same reason. (See Footnote 7).

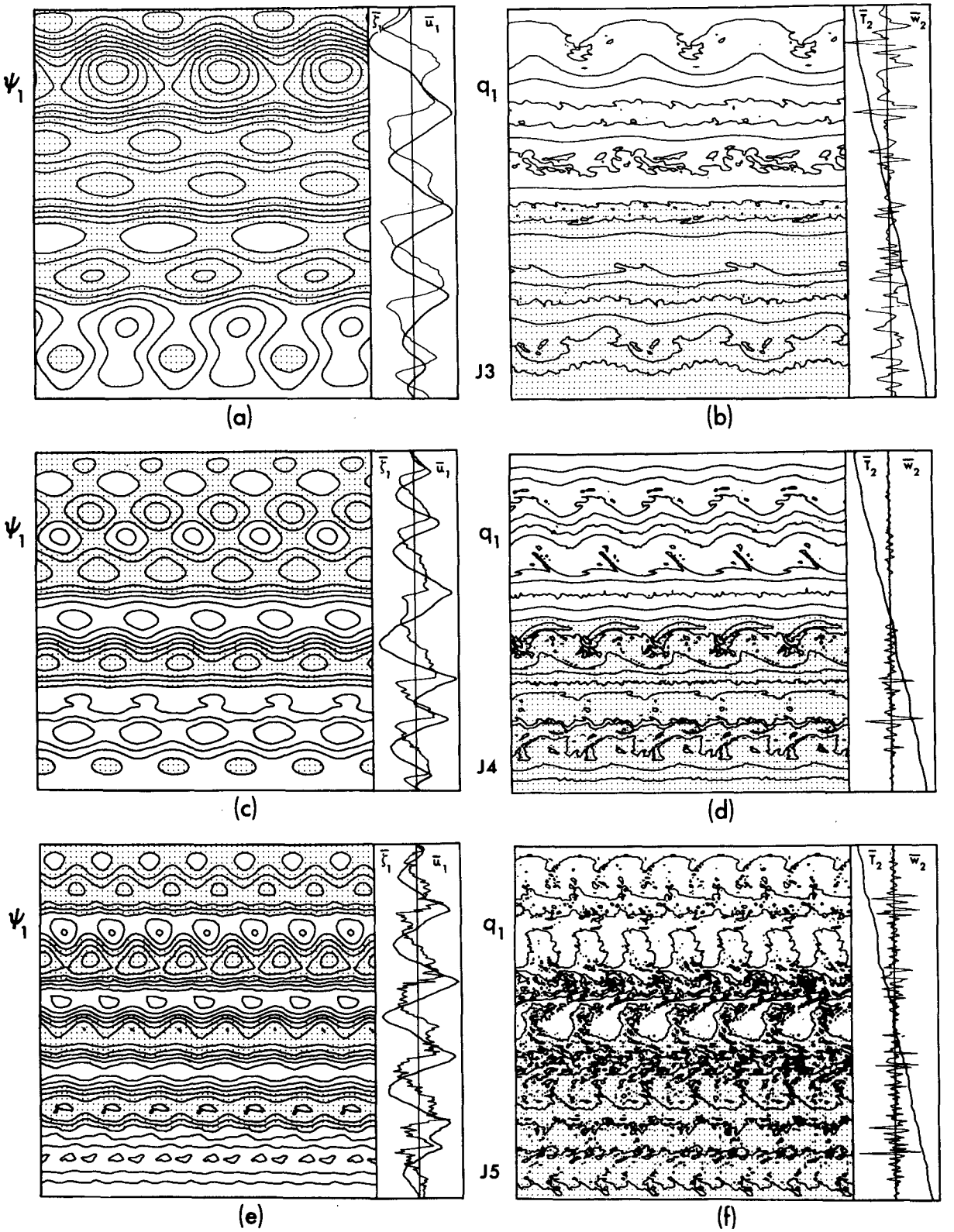

FIG. 20. Case J3 at 586 days (a,b), Case J4 at 402 days (c,d) and Case J5 at 354 days (e,f). Legend as in Fig. 19.

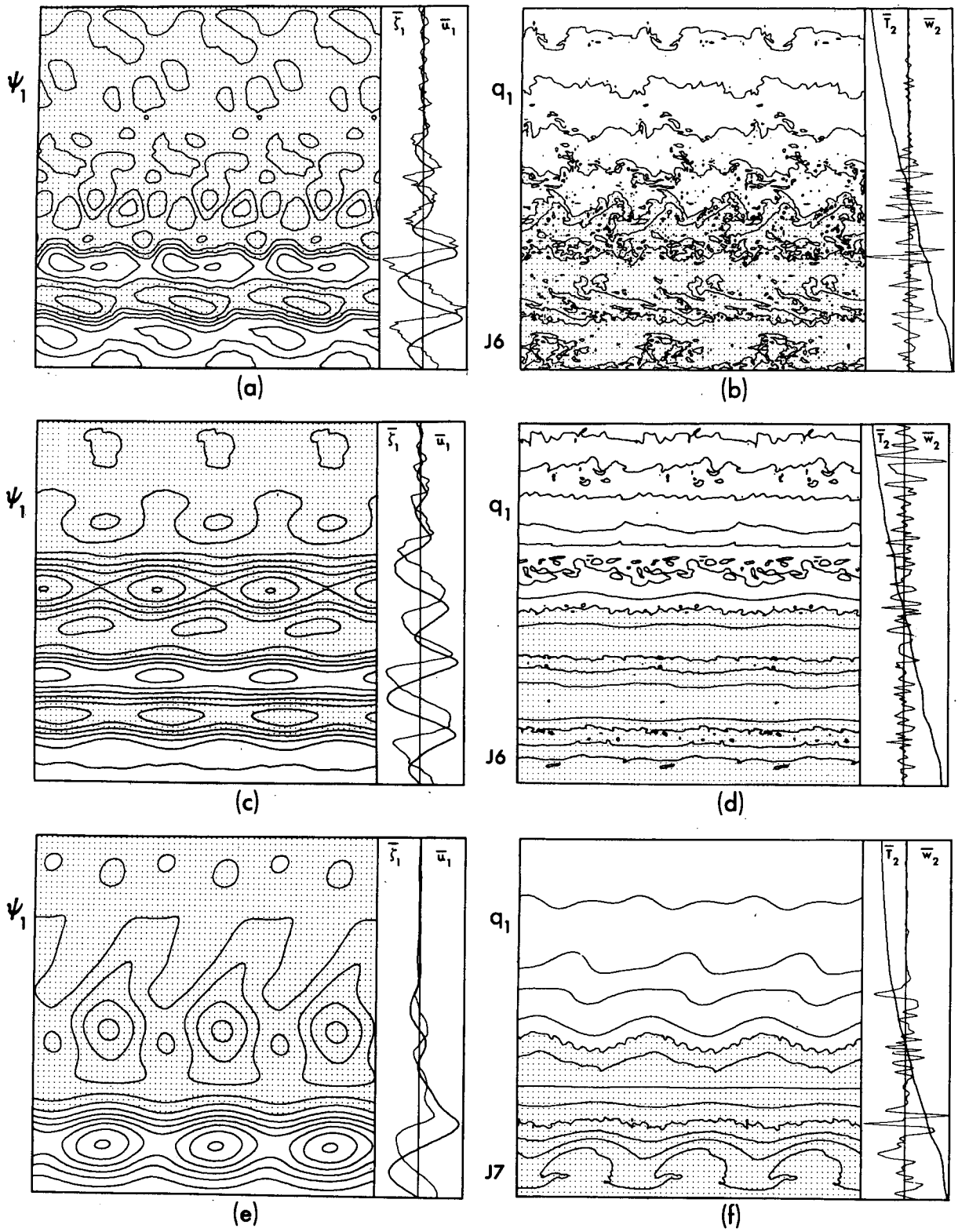

FIG. 21. Case J6 at 196 days (a,b) and 597 days (c,d), and Case J7 at 318 days (e,f). Legend as in Fig. 19. $r=3$.

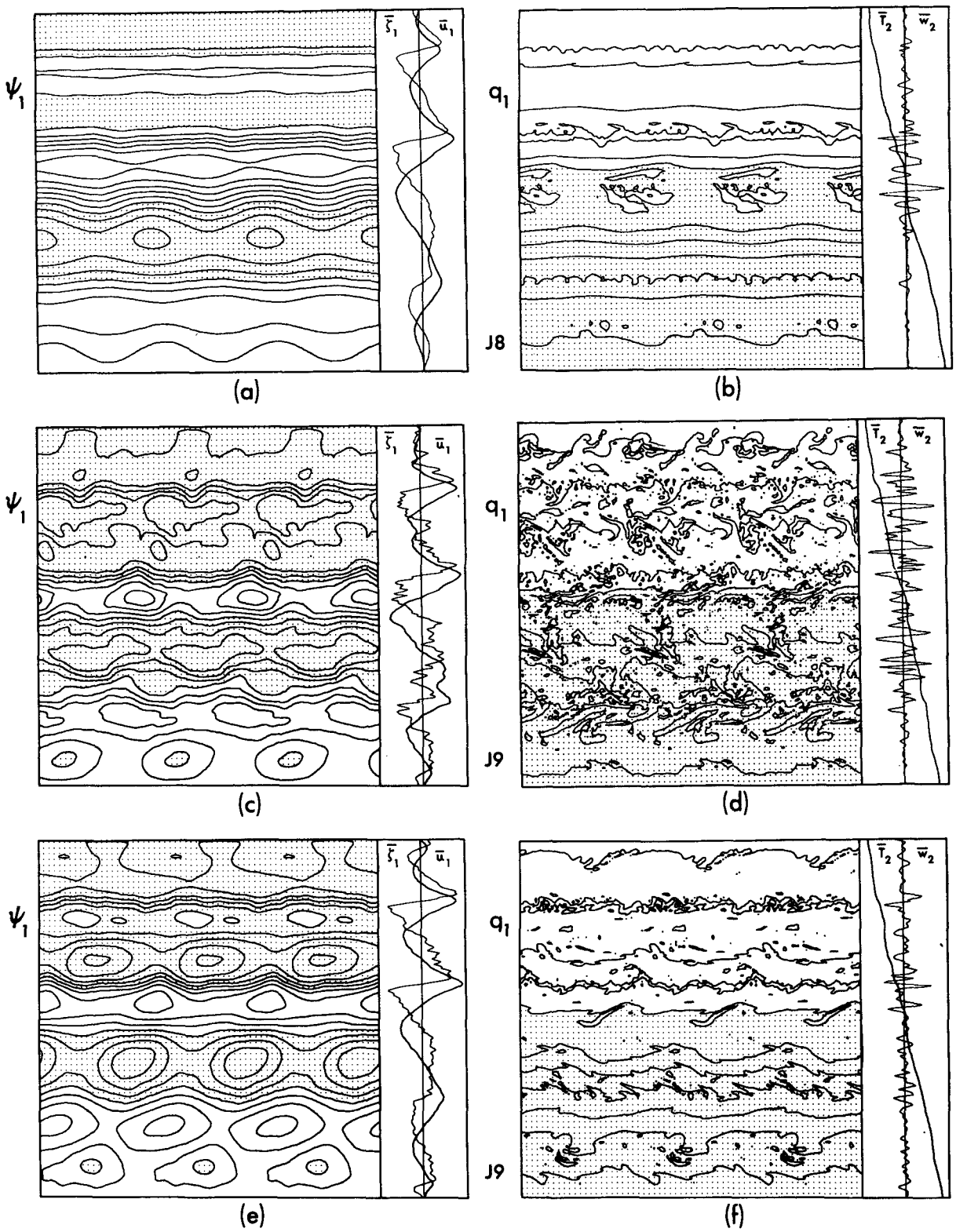

FIG. 22. Case J8 at 1410 days (a,b), and Case J9 at 1137 days (c,d) and 1332 days (e,f). Legend as in Fig. 19. $r=3$.

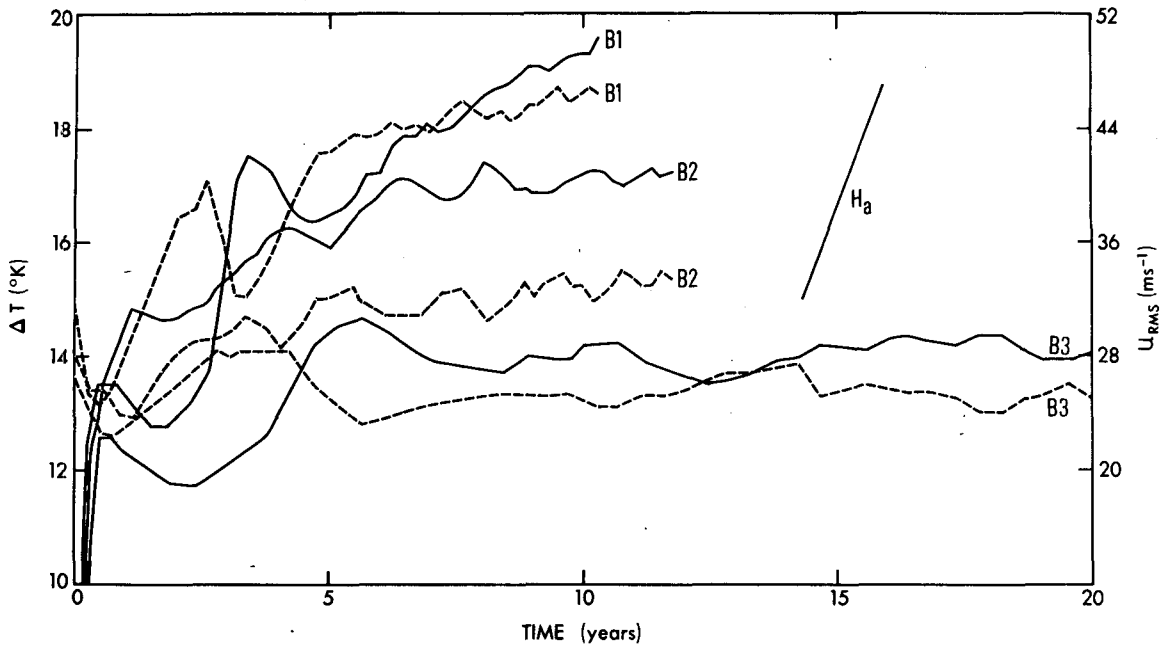

FIG. 23. Cases B1, B2 and B3. Evolution of rms velocity scale U_1 (solid lines) and temperature differential ΔT (dashed lines). Line labeled H_a indicates rate of increase of ΔT that would occur in absence of motion in B1 or B2.

8. Equilibration: B1–B3

The computations to examine the equilibration (rather than the character) of the circulations are equivalent to reevaluating J1 or J8 with a reduced domain size and resolution. The B and J systems have similar multi-jet circulations and equilibration properties.

a. B1: *No drag*

Three westerly jets prevail throughout the B1 calculation. The ΔT, U plots (Fig. 23) show that after the three major energy conversions have occurred, the energy cycle becomes less regular even though both forms of instability still occur. The B1 circulation may be equilibrating but only over a very long time scale.

b. B2: *Weak drag*

The circulation in the B2 case (with its weak surface and interface stresses) has a different evolution from B1 but a similar final form. Moreover, the flow may be equilibrating (Fig. 23). Comparing the final ΔT values for B1 and B2—18.5 and 15.4 K (Table 2)— shows that the eddies reduce the heating gradient by 11 and 13 K. In B2, the reduction almost balances the 14 K baroclinicity generation.[13]

c. B3: *Reduced heating rate*

To be certain that eddies capable of coping with a heating imbalance can be produced, case B2 was recalculated with a heating rate halved to 0.1 units (equivalent to 0.2 units for the J domain). The circulation approaches its quasi-equilibrated, double-jet form in the first 5 years but then fluctuates with a period of about 10 years (Fig. 23). After 20 years, ΔT is 0.4 K less than its initial value and U_1 is less than its value after the initial spinup, i.e., kinetic and thermal equilibration has occurred.

9. Vertical variations: D1

The over-simplified vertical structure of the two-level model limits any analogy between the *baroclinic* aspects of the solutions and Jupiter. To represent properly the decay of activity with depth requires consideration of the depth variation of the static stability and the heating rate.

a. Unequal-layer model

A preliminary estimate of the effect of depth variations in the static stability can be obtained by considering, as in oceanography, a model in which the lower layer is δ times more massive than the upper. The terms $-\lambda_1^2 H f_0^{-1}$ and $\lambda_3^2 H f_0^{-1}$ replace the corresponding ones in the prediction equations (9) and (10), while the q_k are defined as

$$q_1=\nabla^2\psi_1-\lambda_1^2\hat{\psi}, \quad q_3=\nabla^2\psi_3+\lambda_3^2\hat{\psi}, \tag{19}$$

where $\lambda_1^2=\lambda^2(1+\delta)/2$, $\lambda_3^2=\lambda^2(1+\delta^{-1})/2$, with λ^2 now being the mean, p_2-level value. Redefining the barotropic mode as $\hat{\psi}=(\psi_1+\delta\psi_3)/(1+\delta)$ allows the numerical scheme to proceed as before.

[13] The choice of the heating rate for the J cases was based on the apparent equilibration of a prototype B2 calculation.

b. D1: $\delta=4$

As an example of these depth effects, case D1 is calculated with $\delta=4$ (arbitrarily chosen to be as in ocean models) imposed on the B1 system. The static-stability factor has values of $\gamma_1^2=62$ s^2 km^{-2} and $\gamma_3^2=16$ s^2 km^{-2}, so the eddies are smaller in the upper layer.

Although the solution resembles those in the B set, the easterly flows are more barotropic, the energy cycle is less regular and the heat transport is more efficient: after 1427 days, ΔT has risen from 13.7–14.2 K, compared to 16.0 K in B1 (Table 2). These differences are mainly due to the modification of the instability properties by the unequal layering (Gill *et al.*, 1974).

10. Conclusions

Our evaluation of the two-level model supports the hypothesis that quasi-geostrophic circulations with multiple, zonally aligned jets can be *realistically* produced under conditions appropriate to Jupiter and Saturn. The jets result from the interaction of planetary wave propagation and a quasi-geostrophic turbulent cascading that is energized by baroclinic instability—all in the manner imitated by the quasi-two-dimensional cascades examined in Part 1.

The circulations exhibit more than just multiple forms of terrestrial phenomena—there are items peculiar to weakly heated, weakly dissipated multi-jet flows: interjet exchanges by neutral baroclinic waves and energy conversion on two different time and space scales. Absence of an effective surface drag allows the flows to develop far beyond the axisymmetric state, thereby revealing more clearly the evolution of a free atmosphere toward a zonal, barotropic end state—a state whose strength obscures its source (i.e., $|\bar{\psi}|\gg|\hat{\psi}|$) and whose appearance deviates from the terrestrial "norm." Baroclinic aspects of the circulation exhibit their customary form.

Neutral baroclinic waves provide an important adjustment process in a baroclinic fluid and occur naturally, as gyres, in multi-jet circulations.[14] The gyres are analogous in many respects to the Great Red Spot and suggest that the object can be described by the quasi-geostrophic equations. Considerations of longitudinal scale and uniqueness indicate that ultralong baroclinically unstable (Green) waves may provide a closer analogy to the planetary item, but only if the atmosphere is strongly stable.

The cloud formation implied by the solutions is one in which condensation in the bands is correlated (by compression effects) with horizontal variations in the geostrophic pressure. If this is so, then the observed differential rotation of Jupiter's bands indicates geostrophy, not vertical motion. Embedded within the main cloud bands are three-dimensional (eddy) features due to baroclinic instability and frontogenesis.

On Jupiter, the failure to complete the decascade of energy into the zonal mode in polar regions leads to a different regime beyond 50° latitude. This might be occurring because of 1) the lack of baroclinicity in the more uniformly heated polar regions and the consequent low kinetic energy levels, 2) the easier occurrence of (smaller) baroclinically unstable eddies in areas with lower β and higher f_0 values, 3) the reduced wave propagation at lower β values and 4) the non-geostrophy of a convectively-unstable region. However, it is also possible that observations were made during a major instability in which zonality had temporarily disintegrated in high latitudes.

Comparing Saturn with Jupiter, the broader bands and stronger jets—items related by the L_β scale—can be explained, in the quasi-geostrophic view, by a larger static stability or a weaker dissipation. The quasi-steady phases should be longer and the planet generally more quiescent. Detailed observations of Saturn will provide a crucial test of our predictions.

Acknowledgments. The studies described in Parts 1–3 involved many colleagues whose contributions, so freely and ably given, made this work both possible and worthwhile. In particular, I express my thanks to L. Shroyer of Texas Instruments for programming assistance, to T. Reek for graphics advice, to the GFDL computer staff for implementing innumerable jobs, to P. G. Tunison and W. H. Ellis for drafting, to J. N. Connor for photography, and to B. M. Williams for patiently typing and retyping the manuscripts. Conversations with W. B. Rossow helped clarify the ideas on cloud formation and enhanced my understanding of planetary environments. The late R. E. Danielson's enthusiasm for planetary studies was a constant source of encouragement. A special thanks goes to my wife Janet for sustained support during the long evolution of these papers.

APPENDIX A

Reformulation of the Numerical Procedure for the Quasi-Geostrophic Model

The numerical formulation of the quasi-geostrophic model as given by Phillips had defects due to nonlinear instability and overspecification of the boundary conditions. The reformulation given below results in a system that remains computationally stable and physically meaningful indefinitely because of its complete internal consistency.

a. Grid system

The basic variables q_k, ψ_k are discretized at grid points $x=(i-1)\Delta x$, $y=(j-1)\Delta y$ $(i=1, 2, \ldots, M)$, $(j=1, 2, \ldots, L)$, commencing on the lateral walls.

[14] The absence of gyres in the quasi-barotropic multi-jet circulations (see Part 1) indicates that baroclinicity is essential to their existence.

b. Prediction equations

In central difference notation, the prediction equations (9) and (10) become

$$\delta_t\bar{q}_1^t+J(\psi_1,\ f^*+q_1)=\nu(\delta_{xx}+\delta_{yy})q_1-f_0\gamma^2H-\hat{\zeta}/\tau_I, \quad \text{(A1)}$$

$$\delta_t\bar{q}_3^t+J(\psi_3,\ f^*+q_3)=\nu(\delta_{xx}+\delta_{yy})q_3+f_0\gamma^2H+\hat{\zeta}/\tau_I-\zeta_4/\tau_D, \quad \text{(A2)}$$

where $J(\psi,A)\equiv\psi_xA_y-\psi_yA_x$ is the advection Jacobian. All quantities are at the central time level $n\Delta t$ except the diffusion and vertical stress terms which are evaluated at $(n-1)\Delta t$. For the nonlinear terms a form of Arakawa's (1966) Jacobian (45) is used in the interior and a form of his expressions (73) and (74) for predicting q_k on the latitudinal walls; this boundary prediction is necessary to fulfill the kinetic-energy and enstrophy-conserving properties of the Arakawa Jacobian and produce stable solutions.

c. Boundary condition problems

Physical conditions cannot be imposed at the lateral boundaries because of the inherently inviscid nature of the quasi-geostrophic equations. For example, a slip condition $\zeta_B=0$ on the horizontal motion implies [via Eqs. (5) and (6)] a non-slip condition $\omega_B=0$ on the vertical motion; while a non-slip condition $u_B=0$ implies a slipping vertical motion $\omega_B\neq0$ (B denotes a lateral wall value).

We thus opt for quasi-inviscid computational conditions: conditions that give the preferred inviscid scheme when the limit $\nu\to0$ is taken. They are determined by imposing the conservation of vorticity, momentum, mass and heat on the integral form of the finite-difference equations in a manner that neutralizes truncation errors between the ψ_B, q_B variables, yet allows prediction of q_B (to satisfy the Arakawa Jacobian constraints).

d. Integral constraints: Barotropic component

To select the most suitable boundary conditions for the two-level model, the equations must be written in their barotropic and baroclinic forms. The barotropic variables $\bar{\psi}$, $\bar{q}$ control the conservation of vorticity and momentum; their integral equations are

$$\langle\bar{q}_t\rangle=\nu\langle\bar{q}_{yy}\rangle-\langle\zeta_4\rangle/\tau_D, \quad \text{(A3)}$$

$$\bar{\bar{\psi}}_{yy}=\bar{\bar{q}}=\bar{\bar{\zeta}}. \quad \text{(A4)}$$

These equations are subject to the same boundary truncation problems as the quasi-barotropic equations, except that here the drag term contains a baroclinic component. As in Part 1, the wall effects can be neutralized by setting $\nu\bar{q}_y=0$ in the $(\bar{q}_t)_B$ equation and by predicting $\bar{\bar{\psi}}_B$ using the doubly integrated form of (A4) (with the prediction terms substituted for $\bar{\bar{q}}_t$):

$$\bar{\bar{\psi}}_t(Y)-\bar{\bar{\psi}}_t(0)=-[\bar{\psi}_4/\tau_D]_0^Y, \quad \text{(A5)}$$

where the undesirable ν terms have been omitted. These two conditions produce barotropic-vorticity and momentum conservation when $\tau_D\to\infty$.

e. Integral constraints: Baroclinic component

No unique boundary condition exists for the baroclinic component of the quasi-geostrophic equations and the geostrophic relationship between velocity and temperature inhibits a physical choice. Conservation of mass and heat can only be guaranteed by the *baroclinic* variables and computational conditions based on this need are selected, being appropriate to viscous or inviscid fluids.

If the $\hat{q}$, $\hat{\psi}$ equations are not treated in a manner consistent with the equations for ω, $\hat{\zeta}$, there is no guarantee that the diagnostic variables are physically meaningful. Consistency is provided by the baroclinic integral constraints:

$$\langle\hat{q}_t\rangle=\nu\langle\hat{q}_{yy}\rangle-2\langle\hat{\zeta}\rangle/\tau_I+\langle\zeta_4\rangle/\tau_D, \quad \text{(A6)}$$

$$\bar{\bar{\psi}}_{yy}-2\lambda^2\bar{\bar{\psi}}=\bar{\bar{q}}, \quad \text{(A7)}$$

$$\langle\hat{\zeta}_t\rangle=2\frac{f_0}{p_2}\langle\omega_2\rangle+\nu\langle\hat{\zeta}_{yy}\rangle-2\langle\hat{\zeta}\rangle/\tau_I+\langle\zeta_4\rangle/\tau_D, \quad \text{(A8)}$$

$$\frac{f_0}{p_2}\langle\omega_2\rangle=\lambda^2\langle\hat{\psi}_t-\nu\hat{\psi}_{yy}\rangle, \quad \text{(A9)}$$

$$\bar{V}^*(Y)-\bar{V}^*(0)=-\frac{Y}{p_2}\langle\omega_2\rangle. \quad \text{(A10)}$$

To guarantee mass conservation, requires that $\langle\omega_2\rangle=0$ in (A10). This implies heat conservation in (A9) (when $\nu\bar{\bar{\psi}}_{By}=0$) and baroclinic-vorticity conservation in (A8) (when $\nu\bar{\bar{\zeta}}_{By}=0$). These implicit conditions on (A8)–(A10) must be realized indirectly through the $\hat{q}$, $\hat{\psi}$ equations (A6) and (A7), by setting $\nu\hat{q}_{By}=0$ in the $\hat{q}_t$ equation and by summing (A7) over all grid points:

$$\sum_{j=1}^{M}\bar{\hat{q}}_j=\left[\tfrac{1}{2}\bar{\hat{q}}_1+\frac{(\bar{\hat{\psi}}_1-\bar{\hat{\psi}}_2)}{(\Delta y)^2}+\lambda^2\bar{\hat{\psi}}_1\right]+\left[\tfrac{1}{2}\bar{\hat{q}}_L+\frac{(\bar{\hat{\psi}}_L-\bar{\hat{\psi}}_{L-1})}{(\Delta y)^2}+\lambda^2\bar{\hat{\psi}}_L\right], \quad \text{(A11)}$$

where the (undefinable) wall values of $\bar{\hat{\psi}}_{yy}$ are left in the $\bar{\hat{q}}$ form, where $\langle\hat{\psi}\rangle=0$ has been imposed and where indices denote j values. To make (A11) consistent with $\langle\hat{q}_t\rangle=0$, we set each residual boundary term to zero (an arbitrary constant), effectively defining "$\hat{u}_B$"$=0$:

$$\bar{\hat{\psi}}_2-\bar{\hat{\psi}}_1[1+\lambda^2(\Delta y)^2]=\tfrac{1}{2}(\Delta y)^2\bar{\hat{q}}_1, \quad \text{(A12)}$$

$$\bar{\hat{\psi}}_{L-1}-\bar{\hat{\psi}}_L[1+\lambda^2(\Delta y)^2]=\tfrac{1}{2}(\Delta y)^2\bar{\hat{q}}_L. \quad \text{(A13)}$$

A "$\hat{u}_B$"$=0$ condition is the only way of realizing $\bar{V}^*(0)=0$ in the sidewall momentum equation.

f. Eddy boundary conditions

Conditions on the barotropic and baroclinic eddy streamfunctions are identical and straightforward. We set $\psi'_k=0$ to make the sidewalls impermeable to the geostrophic flow.

g. Implementing the boundary conditions

To apply the above constraints, the prediction equations can be used in their fundamental form (A1), (A2) but the Poisson equations must be solved in the barotropic, baroclinic form

$$\nabla^2\bar{\psi}=\bar{q}, \tag{A14}$$

$$(\nabla^2-2\lambda^2)\hat{\psi}=\hat{q}, \tag{A15}$$

with condition (A5) on (A14) and (A12), (A13) on (A15). This method of solution corresponds to the inviscid one—the diffusion terms enter as a computation addendum and do not set the tone of the calculation.

h. Solving the Poisson equations

The technique for solving (A14), (A15) can be described for the general finite difference equation

$$(\delta_{xx}+\delta_{yy}-2\lambda^2)\psi=q, \tag{A16}$$

where for the barotropic case $\lambda\equiv 0$ and a different boundary condition exists for $\bar{\psi}$. To solve (A16), exactly the periodic eigenfunction expansion is made for the x-dependence

$$\psi=\sum_{\alpha=0}^{M-2}\psi^\alpha H_\alpha(i),$$

$$H_\alpha(i)=\Gamma_\alpha\left(\frac{2}{M-1}\right)^{\frac{1}{2}}\cos\left[\frac{2\pi\alpha}{M-1}(i-1)\right]$$

$$\text{for}\quad \alpha=0, 1, \ldots, (M-1)/2,$$

$$H_\alpha(i)=\left(\frac{2}{M-1}\right)^{\frac{1}{2}}\sin\left[\frac{2\pi}{M-1}(i-1)\left(\alpha-\frac{M-1}{2}\right)\right]$$

$$\text{for}\quad \alpha=(M+1)/2, \ldots, M-2, \tag{A17}$$

where $i=1, 2, \ldots, M$, $\Gamma_\alpha=2^{-\frac{1}{2}}$ for $\alpha=0$ and $(M-1)/2$ but $\Gamma_\alpha=1$ for other α.

Substitution of (A17) into (A16) yields

$$\delta_{yy}\psi^\alpha-\left(\frac{\lambda^\alpha}{(\Delta x)^2}+2\lambda^2\right)\psi^\alpha=q^\alpha, \tag{A18}$$

where

$$\lambda^\alpha=\begin{cases}2\left(1-\cos\dfrac{2\pi\alpha}{M-1}\right), & \alpha=0, 1, \ldots, \dfrac{M-1}{2}\\[2ex] 2\left[1-\cos\dfrac{2\pi}{M-1}\left(\alpha-\dfrac{M-1}{2}\right)\right], & \\[2ex] & \alpha=\dfrac{M+1}{2}, \ldots, M-2\end{cases}$$

are the eigenvalues. To solve the difference equation (A18) it is written as

$$-A_j\psi^\alpha_{j+1}+B_j\psi^\alpha_j-C_j\psi^\alpha_{j-1}=D_j, \tag{A19}$$

where

$$A_j=C_j=1,\quad B_j=2[1+\lambda^2(\Delta y)^2]+\lambda^\alpha(\Delta y/\Delta x)^2,$$
$$D_j=-(\Delta y)^2q^\alpha_j.$$

This equation is solved using the backward recursion functions E_j, F_j defined as

$$\psi^\alpha_j=\psi^\alpha_{j+1}E^\alpha_j+F^\alpha_j,\quad E^\alpha_j=(B_j-C_jE^\alpha_{j-1})^{-1},$$
$$F^\alpha_j=E^\alpha_j(D_j+C_jF^\alpha_{j-1}).$$

To apply the boundary conditions the variables are split into mean and eddy form $\psi=\bar{\psi}+\psi'$. For both barotropic and baroclinic eddy components $\psi'=0$ so that $\psi^\alpha=0$ when $\alpha\neq 0$. For the zeroth mode $\psi^0=\bar{\psi}(M-1)^{\frac{1}{2}}$, so the zonal mean conditions (A5) and (A12), (A13) can be implemented. These boundary conditions determine values of E^α_1, F^α_1 for initiating the recursion. The trigometric transform (A17) and its inverse are evaluated using fast Fourier techniques as discussed in Part 1.

i. Diagnostic vertical velocities

Three separate estimates of the vertical velocity can be obtained from Eqs. (5)–(7). When these equations are differenced in the same way as the basic prediction equations (i.e., Arakawa Jacobians are used) then all three sets of ω_2 values are identical (to within roundoff error)—an indication that the formulation is internally consistent and programmed correctly. The magnitude of the roundoff indicates the accuracy to which w_2 is calculated (10^{-9} km s^{-1}).

j. Diagnostic meridional circulation

In the continuum, the lateral boundaries are impermeable to the first order meridional flow only if $\bar{V}^*(0)=0$; however, this condition can only be met *implicitly* by realizing $\bar{u}_{Bt}=0$. The finite-difference scheme does specify such a condition in (A12), (A13) but only to within limits set by boundary truncation errors.

$\bar{V}^*(y)$ is calculated at mid-grid points from the expression

$$\bar{V}^*_{1\,j+\frac{1}{2}} = -\frac{\Delta y}{p_2}\left(\tfrac{1}{2}\bar{\omega}_{j=1} + \sum_{j=2} \bar{\omega}_j\right), \qquad \text{(A20)}$$

with $\bar{V}^*_{3j} = -\bar{V}^*_{1j}$. The upper boundary condition $\bar{V}^*(Y) = 0$ is achieved through the implicit conservation of $\langle\omega_2\rangle$ by the prediction equations.

k. Diagnostic momentum balance

The equations for mean momentum changes in the two layers,

$$\bar{u}_{1t} = -\overline{(u_1'v_1')}_y + f_0\bar{V}^*_1 + \nu\bar{u}_{1yy} - \bar{u}/\tau_I, \qquad \text{(A21)}$$

$$\bar{u}_{3t} = -\overline{(u_3'v_3')}_y + f_0\bar{V}^*_3 + \nu\bar{u}_{3yy} + \bar{u}/\tau_I - \bar{u}_4/\tau_D, \qquad \text{(A22)}$$

are calculated using finite-difference forms related to the prediction equations, i.e., from the corresponding terms of

$$-\int_0^y \bar{\zeta}_{kt}\,dy.$$

In particular, the nonlinear term is very sensitive to its formulation and is best calculated as

$$\int_0^y J(\psi,\zeta)\,dy$$

using the Arakawa Jacobian.

The zonal velocity can be accurately defined for the fluid interior but truncation errors in defining u_B affect the indirect realization of $\bar{V}^*(0) = 0$, which in turn disrupts the otherwise accurate estimates of the interior momentum balances; however, the inaccuracy has no dynamical consequence.

l. Diagnostic heat balance

The equation for the mean temperature change,

$$\bar{T}_{2t} = -\overline{(v_2'T_2')}_y + \frac{H}{R} + \frac{\bar{\omega}_2}{\gamma^2 R p_2} + \nu\bar{T}_{2yy}, \qquad \text{(A23)}$$

involves the inverse of the calculation made to obtain $\bar{\omega}_2$ and as such is identically satisfied if the same numerical expressions are adhered to. The equation thus contains no numerical diagnostic.

m. Diagnostic energy balance

The mean and eddy kinetic energies $\bar{K}$, K' and potential energies $\bar{P}$, P' have an energy exchange scheme that can be written as

$$\bar{K}_t = \{\bar{P}\bar{K}\} + \{K'\bar{K}\} - \{\bar{K}F\} - \{\bar{K}D\} - \{\bar{K}I\}, \qquad \text{(A24)}$$

$$K'_t = \{P'K'\} - \{K'\bar{K}\} - \{K'F\} - \{K'D\} - \{K'I\}, \qquad \text{(A25)}$$

$$\bar{P}_t = -\{\bar{P}\bar{K}\} - \{\bar{P}P'\} + \{Q\bar{P}\} - \{\bar{P}F\}, \qquad \text{(A26)}$$

$$P'_t = -\{P'K'\} + \{\bar{P}P'\} - \{P'F\}, \qquad \text{(A27)}$$

where Q, F, D and I denote changes related to heating, lateral diffusion, surface drag and interface stress, respectively. Domain means rather than totals are calculated. By formulating the individual terms in relation to the basic q, ψ equations, exact balances can be achieved in the finite-difference form. However, this does not necessarily indicate numerical accuracy because the basic potential energy equations effectively involve an identity—as in (A23)—and the kinetic energy equations are likewise identities if they use values of ω_2 derived from the ζ_t equations. The only valid numerical check comes from comparing the conversion terms $\{\bar{P}\bar{K}\}$, $\{P'K'\}$ on calculating them in separate ways, but this is essentially the same as comcomparing the three ω_2 estimates.

The various terms are listed below in forms related to the prediction equations. Each variable is at the central time level n, unless noted to the contrary, and the k indices denote sums for both levels.

(i)
$$\bar{P} = \tfrac{1}{2}\lambda^2\langle\hat{\psi}^2\rangle$$

$$\bar{P}_t = \lambda^2\langle\bar{\hat{\psi}}_t\bar{\hat{\psi}}\rangle$$

$$\{Q\bar{P}\} = \frac{\lambda^2}{f_0}\langle H\hat{\psi}\rangle$$

$$\{\bar{P}P'\} = \lambda^2\langle\bar{\hat{\psi}}\bar{J}(\psi_1,\hat{\psi})\rangle$$

$$\{\bar{P}\bar{K}\} = -\frac{f_0}{p_2}\langle\bar{\omega}_2\bar{\hat{\psi}}\rangle \text{ with } \omega_2 \text{ based on (7)}$$

$$\{\bar{P}F\} = -\nu\lambda^2\langle\bar{\hat{\psi}}\bar{\hat{\psi}}^{n-1}_{yy}\rangle.$$

(ii)
$$P' = \tfrac{1}{2}\lambda^2\langle\hat{\psi}'^2\rangle$$

$$P'_t = \lambda^2\langle\hat{\psi}'_t\hat{\psi}'\rangle$$

$$\{P'K'\} = -\frac{f_0}{p_2}\langle\omega_2'\hat{\psi}'\rangle \text{ with } \omega_2 \text{ based on (7)}$$

$$\{P'F\} = -\nu\lambda^2\langle\hat{\psi}'(\nabla^2\hat{\psi}')^{n-1}\rangle.$$

(iii)
$$\bar{K} = -\langle\bar{\psi}_k\bar{\zeta}_k\rangle$$

$$\bar{K}_t = -\langle\bar{\psi}_k\bar{\zeta}_{kt}\rangle$$

$$\{\bar{P}\bar{K}\} = -\frac{f_0}{p_2}\langle\bar{\omega}_2\bar{\hat{\psi}}\rangle \text{ with } \omega_2 \text{ based on (5), (6)}$$

$$\{K'\bar{K}\} = \langle\bar{\psi}_k\bar{J}(\psi_k,\zeta_k)\rangle$$

$$\{\bar{K}F\} = \nu\langle\bar{\psi}_k\bar{\zeta}^{n-1}_{kyy}\rangle$$

$$\{\bar{K}I\} = -\tau_I^{-1}\langle\bar{\psi}_2\bar{\zeta}^{n-1}_2\rangle$$

$$\{\bar{K}D\} = -\tau_D^{-1}\langle\bar{\psi}_3\bar{\zeta}^{n-1}_4\rangle.$$

(iv) $K' = -\langle \psi'_k \zeta'_k \rangle$

$K'_t = -\langle \psi'_k \zeta'_{kt} \rangle$

$\{P'K'\} = -\frac{f_0}{p_2}\langle \omega'_2 \hat{\psi}' \rangle$ with ω_2 based on (5), (6)

$\{K'F\} = \nu \langle \psi'_k (\nabla^2 \zeta')^{n-1}_k \rangle$

$\{K'I\} = -\tau_I^{-1} \langle \hat{\psi}' \hat{\zeta}'^{n-1} \rangle$

$\{K'D\} = -\tau_D^{-1} \langle \psi'_3 \zeta'^{n-1}_4 \rangle$.

The definition of kinetic energy from the product $\psi\zeta$ involves a transformation with boundary terms that can be written

$$\bar{\psi}_1 \bar{\psi}_{1y} + \bar{\psi}_3 \bar{\psi}_{3y} = \tfrac{1}{2}(\bar{\hat{\psi}}\bar{\hat{\psi}}_y + \bar{\hat{\psi}}\bar{\hat{\psi}}_y)$$

for the layered case. Our choice of boundary conditions $\bar{\hat{\psi}}_B = 0$ (when $\tau_D = \infty$) and "$\bar{\hat{\psi}}_{By}$"$= 0$ indicates that this term is insignificant, zero except for unavoidable boundary truncation contributions—in practice it is always less than 10^{-4} of the kinetic energy.

n. Accuracy level

The problem of calculating small predictors (see Part I) becomes more acute for the higher resolutions and weaker heating rates of the Jovian calculations compared to the terrestrial ones. Nonetheless, accurate solutions are obtained. For example, at the end of the J1 calculation the domain means of $\langle w \rangle \sim 10^{-9}$ km s^{-1}, $\langle u \rangle \sim 10^{-7}$ km s^{-1}, $\langle T \rangle \sim 10^{-2}$ K, $\langle q \rangle \sim 10^{-7}$ s^{-1} lie well below the average value of each variable; thus, basic items are adequately conserved.

In the identity $\hat{q} = \hat{\zeta} - 2\lambda^2 \hat{\psi}$, the terms are of the order of 10^{-5}, 10^{-7}, 10^{-5} s^{-1} so the motion-dependent diagnostics lose two decimal places of accuracy (the machine has 6). The upper boundary value of $\bar{V}^*(y)$ $\sim 10^{-6}$ km s^{-1} is satisfactorily small.

o. Computational procedure

The calculations are carried out in the traditional manner established by Phillips (1956). First, an axisymmetric state is generated until a supercritical temperature differential exists. Then a random perturbation of the barotropic eddy field $\tilde{q}'^{n+1}$ (prior to the ψ^{n+1} calculation) induces three-dimensional motion without disturbing integrals or consistency.

Extrapolation of (A1), (A2) by the leapfrog scheme is governed by the advective time-step criterion $\Delta t < (\Delta x/|u| + \Delta y/|v|)^{-1}$. For efficiency, optimum Δt values are used, being reduced in value as the energy level rises.

APPENDIX B

Supplementary Figure Legends

FIG. 4. Case J1 at 43 days. Basic fields and profiles. Fields are streamfunction, potential vorticity, eddy streamfunction, vertical velocity, vertical streamfunction differential (temperature) and vorticity in (a)–(f), respectively; indices denote pressure level, abscissa $x=0$, X, ordinate $y=0$, Y; field is denoted by contour interval, e.g., $\Delta\psi$, in (a), with zero and negative values shaded by selection of gridpoints. On right hand side, zonal mean fields have scales denoted by asterisked values, with zero value at center, e.g., $\bar{u}(y)$ indicated from $-u_1^*$ at left boundary to $+u_1^*$ at right boundary; heavy-line profile is listed before light one. ($T_{z_{y'}}$ denotes temperature difference between grid points).

(a)	$\Delta\psi_1 = 20$ km^2 s^{-1},	$u_1^* = 5$ m s^{-1},	$\zeta_2^* = 5\times10^{-7}$ s^{-1}
(b)	$\Delta q_1 = 4\times10^{-5}$ s^{-1},	$T_2^* = 20$ K,	$w_2^* = 5\times10^{-8}$ km s^{-1}
(c)	$\Delta\psi'_1 = 2$ km^2 s^{-1},	$T_{2y'}^* = 0.2$ K,	$\lvert w'_2\rvert^* = 1\times10^{-6}$ km s^{-1}
(d)	$\Delta w_2 = 5\times10^{-7}$ km s^{-1},	$u_1^* = 5$ m s^{-1},	$\zeta_2^* = 5\times10^{-7}$ s^{-1},
(e)	$\Delta\hat{\psi}_2 = 10$ km^2 s^{-1},	$T_2^* = 20$ K,	$w_2^* = 5\times10^{-8}$ km s^{-1}
(f)	$\Delta\zeta_2 = 2\times10^{-6}$ s^{-1},	$u_1^* = 5$ m s^{-1},	$u_3^* = 5$ m s^{-1}.

FIG. 5. Case J1 at 58 days. Variables and notation as in Fig. 4. A denotes jet formation area discussed in text.

(a)	$\Delta\psi_1 = 20$ km^2 s^{-1},	$u_1^* = 15$ m s^{-1},	$\zeta_2^* = 7\times10^{-6}$ s^{-1}
(b)	$\Delta q_1 = 4\times10^{-5}$ s^{-1},	$T_2^* = 20$ K,	$w_2^* = 1.2\times10^{-6}$ km s^{-1}
(c)	$\Delta\psi'_1 = 10$ km^2 s^{-1},	$T_{2y'}^* = 0.2$ K,	$\lvert w'_2\rvert^* = 5\times10^{-6}$ km s^{-1}
(d)	$\Delta w_2 = 3\times10^{-6}$ km s^{-1},	$u_1^* = 15$ m s^{-1},	$\zeta_2^* = 7\times10^{-6}$ s^{-1}
(e)	$\Delta\hat{\psi}_2 = 15$ km^2 s^{-1},	$T_2^* = 20$ K,	$w_2^* = 1.2\times10^{-6}$ km s^{-1}
(f)	$\Delta\zeta_2 = 1.5\times10^{-5}$ s^{-1},	$u_1^* = 15$ m s^{-1},	$u_3^* = 15$ m s^{-1}.

FIG. 6. Case J1 at 104 days, legend as in Fig. 4.

(a)	$\Delta\psi_1=30$ km^2 s^{-1},	$u_1^*=22$ m s^{-1},	$\zeta_2^*=1.1\times10^{-5}$ s^{-1}
(b)	$\Delta q_1=5\times10^{-5}$ s^{-1},	$T_2^*=20$ K,	$w_2^*=1.2\times10^{-6}$ km s^{-1}
(c)	$\Delta\psi_1'=30$ km^2 s^{-1},	$T_{2y'}^*=0.25$ K,	$\lvert w_2'\rvert^*=6\times10^{-6}$ km s^{-1}
(d)	$\Delta w_2=8\times10^{-6}$ km s^{-1},	$u_1^*=22$ m s^{-1},	$\zeta_2^*=1.1\times10^{-5}$ s^{-1}
(e)	$\Delta\hat{\psi}_2=16$ km^2 s^{-1},	$T_2^*=20$ K,	$w_2^*=1.2\times10^{-6}$ km s^{-1}
(f)	$\Delta\zeta_2=1.5\times10^{-5}$ s^{-1},	$u_1^*=22$ m s^{-1},	$u_3^*=22$ m s^{-1}.

FIG. 7. Case J1 at 178 days, legend as in Fig. 4.

(a)	$\Delta\psi_1=40$ km^2 s^{-1},	$u_1^*=50$ m s^{-1},	$\zeta_2^*=2\times10^{-5}$ s^{-1}
(b)	$\Delta q_1=4\times10^{-5}$ s^{-1},	$T_2^*=20$ K,	$w_2^*=7\times10^{-7}$ km s^{-1}
(c)	$\Delta\psi_1'=40$ km^2 s^{-1},	$T_{2y'}^*=0.4$ K,	$\lvert w_2'\rvert^*=6\times10^{-6}$ km s^{-1}
(d)	$\Delta w_2=8\times10^{-6}$ km s^{-1},	$u_1^*=50$ m s^{-1},	$\zeta_2^*=2\times10^{-5}$ s^{-1}
(e)	$\Delta\hat{\psi}_2=16$ km^2 s^{-1},	$T_2^*=20$ K,	$w_2^*=7\times10^{-7}$ km s^{-1}
(f)	$\Delta\zeta_2=1.5\times10^{-5}$ s^{-1},	$u_1^*=50$ m s^{-1},	$u_3^*=50$ m s^{-1}.

FIG. 8. Case J1 at 316 days, legend as in Fig. 4.

(a)	$\Delta\psi_1=40$ km^2 s^{-1},	$u_1^*=50$ m s^{-1},	$\zeta_2^*=1.5\times10^{-5}$ s^{-1}
(b)	$\Delta q_1=3\times10^{-5}$ s^{-1},	$T_2^*=20$ K,	$w_2^*=2.5\times10^{-7}$ km s^{-1}
(c)	$\Delta\psi_1'=20$ km^2 s^{-1},	$T_{2y'}^*=0.35$ K,	$\lvert w_2'\rvert^*=1.6\times10^{-6}$ km s^{-1}
(d)	$\Delta w_2=1.5\times10^{-6}$ km s^{-1},	$u_1^*=50$ m s^{-1},	$\zeta_2^*=1.5\times10^{-5}$ s^{-1}
(e)	$\Delta\hat{\psi}_2=16$ km^2 s^{-1},	$T_2^*=20$ K,	$w_2^*=2.5\times10^{-7}$ km s^{-1}
(f)	$\Delta\zeta_2=8\times10^{-6}$ s^{-1},	$u_1^*=50$ m s^{-1},	$u_3^*=50$ m s^{-1}.

FIG. 9. Case J1 at 591 days, legend as in Fig. 4.

(a)	$\Delta\psi_1=40$ km^2 s^{-1},	$u_1^*=60$ m s^{-1},	$\zeta_2^*=2\times10^{-5}$ s^{-1}
(b)	$\Delta q_1=3\times10^{-5}$ s^{-1},	$T_2^*=20$ K,	$w_2^*=5\times10^{-8}$ km s^{-1}
(c)	$\Delta\psi_1'=20$ km^2 s^{-1},	$T_{2y'}^*=0.3$ K,	$\lvert w_2'\rvert^*=8\times10^{-7}$ km s^{-1}
(d)	$\Delta w_2=5\times10^{-7}$ km s^{-1},	$u_1^*=60$ m s^{-1},	$\zeta_2^*=2\times10^{-5}$ s^{-1}
(e)	$\Delta\hat{\psi}_2=16$ km^2 s^{-1},	$T_2^*=20$ K,	$w_2^*=5\times10^{-8}$ km s^{-1}
(f)	$\Delta\zeta_2=5\times10^{-6}$ s^{-1},	$u_1^*=60$ m s^{-1},	$u_3^*=60$ m s^{-1}.

FIG. 11. Case J1 at 1306 days, legend as in Fig. 4.

(a)	$\Delta\psi_1=60$ km^2 s^{-1},	$u_1^*=100$ m s^{-1},	$\zeta_2^*=2\times10^{-5}$ s^{-1}
(b)	$\Delta q_1=6\times10^{-5}$ s^{-1},	$T_2^*=25$ K,	$w_2^*=2\times10^{-6}$ km s^{-1}
(c)	$\Delta\psi_1'=60$ km s^{-1},	$T_{2y'}^*=25$ K,	$\lvert w_2'\rvert^*=1.2\times10^{-5}$ km s^{-1}
(d)	$\Delta w_2=1\times10^{-5}$ km s^{-1},	$u_1^*=100$ m s^{-1},	$\zeta_2^*=2\times10^{-5}$ s^{-1}
(e)	$\Delta\hat{\psi}_2=20$ km^2 s^{-1},	$T_2^*=25$ K,	$w_2^*=2\times10^{-6}$ km s^{-1}
(f)	$\Delta\zeta_2=3\times10^{-5}$ s^{-1},	$u_1^*=100$ m s^{-1},	$u_3^*=100$ m s^{-1}.

FIG. 12. Case J1 at 1392 days, legend as in Fig. 4.

(a)	$\Delta\psi_1=100$ km^2 s^{-1},	$u_1^*=100$ m s^{-1},	$\zeta_2^*=3\times10^{-5}$ s^{-1}
(b)	$\Delta q_1=1.2\times10^{-4}$ s^{-1},	$T_2^*=25$ K,	$w_2^*=2\times10^{-5}$ km s^{-1}
(c)	$\Delta\psi_1'=60$ km^2 s^{-1},	$T_{2y'}^*=0.7$ K,	$\lvert w_2'\rvert^*=6\times10^{-5}$ km s^{-1}
(d)	$\Delta w_2=5\times10^{-5}$ km s^{-1},	$u_1^*=100$ m s^{-1},	$\zeta_2^*=3\times10^{-5}$ s^{-1}
(e)	$\Delta\hat{\psi}_2=30$ km^2 s^{-1},	$T_2^*=25$ K,	$w_2^*=2\times10^{-5}$ km s^{-1}
(f)	$\Delta\zeta_2=4\times10^{-5}$ s^{-1},	$u_1^*=100$ m s^{-1},	$u_3^*=100$ m s^{-1}.

FIG. 13. Case J1 at 1471 days, legend as in Fig. 4.

(a)	$\Delta\psi_1=120$ km^2 s^{-1},	$u_1^*=150$ m s^{-1},	$\zeta_2^*=4\times10^{-5}$ s^{-1}
(b)	$\Delta q_1=1.2\times10^{-4}$ s^{-1},	$T_2^*=25$ K,	$w_2^*=1\times10^{-5}$ km s^{-1}
(c)	$\Delta\psi_1'=80$ km^2 s^{-1},	$T_{2y'}^*=0.7$ K,	$\lvert w_2'\rvert^*=4\times10^{-5}$ km s^{-1}
(d)	$\Delta w_2=5\times10^{-5}$ km s^{-1},	$u_1^*=150$ m s^{-1},	$\zeta_2^*=4\times10^{-5}$ s^{-1}
(e)	$\Delta\hat{\psi}_2=30$ km^2 s^{-1},	$T_2^*=25$ K,	$w_2^*=1\times10^{-5}$ km s^{-1}
(f)	$\Delta\zeta_2=5\times10^{-5}$ s^{-1},	$u_1^*=150$ m s^{-1},	$u_2^*=150$ m s^{-1}.

FIG. 14. Case J1 at 1773 days, legend as in Fig. 4.

(a)	$\Delta\psi_1=150$ km^2 s^{-1},	$u_1^*=160$ m s^{-1},	$\zeta_2^*=4\times10^{-5}$ s^{-1}
(b)	$\Delta q_1=4\times10^{-5}$ s^{-1},	$T_2^*=30$ K,	$w_2^*=7\times10^{-7}$ km s^{-1}
(c)	$\Delta\psi_1'=30$ km^2 s^{-1},	$T_{2v'}^*=0.7$ K,	$\lvert w_2'\rvert^*=8\times10^{-6}$ km s^{-1}
(d)	$\Delta w_2=8\times10^{-6}$ km s^{-1},	$u_1^*=160$ m s^{-1},	$\zeta_2^*=4\times10^{-5}$ s^{-1}
(e)	$\Delta\hat{\psi}_2=20$ km^2 s^{-1},	$T_2^*=30$ K,	$w_2^*=7\times10^{-7}$ km s^{-1}
(f)	$\Delta\zeta_2=1.5\times10^{-5}$ s^{-1},	$u_1^*=160$ m s^{-1},	$u_3^*=160$ m s^{-1}.

FIG. 15. Case J1 at 2184 days, legend as in Fig. 4.

(a)	$\Delta\psi_1=150$ km^2 s^{-1},	$u_1^*=130$ m s^{-1},	$\zeta_2^*=2\times10^{-5}$ s^{-1}
(b)	$\Delta q_1=4\times10^{-5}$ s^{-1},	$T_2^*=30$ K,	$w_2^*=1\times10^{-7}$ km s^{-1}
(c)	$\Delta\psi_1'=20$ km^2 s^{-1},	$T_{2v'}^*=0.5$ K,	$\lvert w_2'\rvert^*=1.2\times10^{-6}$ km s^{-1}
(d)	$\Delta w_2=7\times10^{-7}$ km s^{-1},	$u_1^*=130$ m s^{-1},	$\zeta_2^*=2\times10^{-5}$ s^{-1}
(e)	$\Delta\hat{\psi}_2=20$ km^2 s^{-1},	$T_2^*=30$ K,	$w_2^*=1\times10^{-7}$ km s^{-1}
(f)	$\Delta\zeta_2=5\times10^{-6}$ s^{-1},	$u_1^*=130$ m s^{-1},	$u_3^*=130$ m s^{-1}.

FIG. 20. Case J3 at 586 days (a,b); Case J4 at 402 days (c,d) and Case J5 at 354 days (e,f). Legend as in Fig. 19.

(a)	$\Delta\psi_1=80$ km^2 s^{-1},	$u_1^*=60$ m s^{-1},	$\zeta_2^*=1.5\times10^{-5}$ s^{-1}, $r=3$
(b)	$\Delta q_1=7\times10^{-5}$ s^{-1},	$T_2^*=10$ K,	$w_2^*=1.5\times10^{-7}$ km s^{-1}, $r=3$
(c)	$\Delta\psi_1=80$ km^2 s^{-1},	$u_1^*=60$ m s^{-1},	$\zeta_2^*=3\times10^{-5}$ s^{-1}, $r=5$
(d)	$\Delta q_1=8\times10^{-5}$ s^{-1},	$T_2^*=10$ K,	$w_2^*=2\times10^{-6}$ km s^{-1}, $r=5$
(e)	$\Delta\psi_1=80$ km^2 s^{-1},	$u_1^*=80$ m s^{-1},	$\zeta_2^*=4\times10^{-5}$ s^{-1}, $r=7$
(e)	$\Delta q_1=2\times10^{-4}$ s^{-1},	$T_2^*=6$ K,	$w_2^*=1\times10^{-5}$ km s^{-1}, $r=7$.

FIG. 21. Case J6 at 196 days (a,b) and 597 days (c,d), and Case J7 at 318 days (e,f). Legend as in Fig. 19. $r=3$.

(a)	$\Delta\psi_1=80$ km^2 s^{-1},	$u_1^*=70$ m s^{-1},	$\zeta_2^*=2\times10^{-5}$ s^{-1}
(b)	$\Delta q_1=1\times10^{-4}$ s^{-1},	$T_2^*=10$ K,	$w_2^*=2\times10^{-6}$ km s^{-1}
(c)	$\Delta\psi_1=80$ km^2 s^{-1},	$u_1^*=70$ m s^{-1},	$\zeta_2^*=2\times10^{-5}$ s^{-1}
(d)	$\Delta q_1=8\times10^{-5}$ s^{-1},	$T_2^*=15$ K,	$w_2^*=2\times10^{-7}$ km s^{-1}
(e)	$\Delta\psi_1=150$ km^2 s^{-1},	$u_1^*=100$ m s^{-1},	$\zeta_2^*=3\times10^{-5}$ s^{-1}
(f)	$\Delta q_1=8\times10^{-5}$ s^{-1},	$T_2^*=12$ K,	$w_2^*=1.6\times10^{-7}$ km s^{-1}

FIG. 22. Case J8 at 1410 days (a,b), and Case J9 at 1137 days (c,d) and 1332 days (e,f). Legend as in Fig. 19. $r=3$.

(a)	$\Delta\psi_1=200$ km^2 s^{-1},	$u_1^*=200$ m s^{-1},	$\zeta_2^*=4\times10^{-5}$ s^{-1}
(b)	$\Delta q_1=8\times10^{-5}$ s^{-1},	$T_2^*=25$ K,	$w_2^*=4\times10^{-7}$ km s^{-1}
(c)	$\Delta\psi_1=120$ km^2 s^{-1},	$u_1^*=100$ m s^{-1},	$\zeta_2^*=3\times10^{-5}$ s^{-1}
(d)	$\Delta q_1=12\times10^{-5}$ s^{-1},	$T_2^*=25$ K,	$w_2^*=4\times10^{-6}$ km s^{-1}
(e)	$\Delta\psi_1=120$ km^2 s^{-1},	$u_1^*=120$ m s^{-1},	$\zeta_2^*=3\times10^{-5}$ s^{-1}
(f)	$\Delta q_1=8\times10^{-5}$ s^{-1},	$T_2^*=25$ K,	$w_2^*=2\times10^{-6}$ km s^{-1}.

REFERENCES

Arakawa, A., 1966: Computational design for long-term numerical integration of the equations of fluid motion. *J. Comput. Phys.*, **1**, 119–143.

Charney, J. G., 1959: On the general circulation of the atmosphere. *The Atmosphere and Sea in Motion*, B. Bolin, Ed., Rockefeller Institute Press, 178–193.

Gehrels, T., 1976: The results of the imaging photopolarimeter on Pioneers 10 and 11. *Jupiter*, T. Gehrels, Ed., University of Arizona Press, 531–563.

Gill, A. E., J. S. A. Green and A. J. Simmons, 1974: Energy partition in the large-scale ocean circulation and the production of mid-ocean eddies. *Deep-Sea Res.*, **21**, 499–528.

Green, J. S. A., 1960: A problem in baroclinic stability. *Quart. J. Roy. Meteor. Soc.*, **86**, 237–251.

Hirota, I., 1968: On the dynamics of long and ultra-long waves in a baroclinic zonal current. *J. Meteor. Soc. Japan*, **46**, 234–249.

Kuo, H-L., 1951: Vorticity transfer as related to the development of the general circulation. *J. Meteor.*, **8**, 307–315.

Mahlman, J. D., and W. J. Moxim, 1978: Tracer simulation using a global general circulation model: Results from a mid-latitude instantaneous source experiment. *J. Atmos. Sci.*, **35**, 1340–1374.

McIntyre, M. E., 1972: Baroclinic instability of an idealized model of the polar night jet. *Quart. J. Roy. Meteor. Soc.*, **98**, 165–174.

Merkine, L-O., 1977: Convective and absolute instability of baroclinic eddies. *Geophys. Astrophys. Fluid Dyn.*, **9**, 129–157.

Pedlosky, J., 1964: The stability of currents in the atmosphere and the ocean. Part 1. *J. Atmos. Sci.*, **21**, 201–219.

Peek, B. M., 1958: *The Planet Jupiter*. Faber and Faber, 283 pp.

Philander, S. G. H., 1978: Forced oceanic waves. *Rev. Geophys. Space Phys.*, **16**, 15–46.

Phillips, N. A., 1954: Energy transformations and meridional circulations associated with simple baroclinic waves in a two-level, quasi-geostrophic model. *Tellus*, **6**, 273–286.

——, 1956: The general circulation of the atmosphere: a numerical experiment. *Quart. J. Roy. Meteor. Soc.*, **82**, 123–164.

——, 1963: Geostrophic motion. *Rev. Geophys.* **1**, 123–176.

Rhines, P. B., 1975: Waves and turbulence on a beta plane. *J. Fluid Mech.*, **69**, 417–443.

Rossow, W. B., 1978: Cloud microphysics: Analysis of the clouds of Earth, Venus, Mars and Jupiter. *Icarus*, **36**, 1–50.

Schneider, S. H., and R. E. Dickinson, 1974: Climate modeling. *Rev. Geophys. Space Phys.*, **12**, 447–493.

Simmons, A. J., 1974: The meridional scale of baroclinic waves. *J. Atmos. Sci.*, **31**, 1515–1525.

Stone, P. H., 1969: The meridional structure of baroclinic waves. *J. Atmos. Sci.*, **26**, 376–389.

——, 1972: A simplified radiative-dynamical model for the static stability of rotating atmospheres. *J. Atmos. Sci.*, **29**, 405–418.

——, 1976: The meteorology of the Jovian atmosphere. *Jupiter*, T. Gehrels Ed., University of Arizona Press, 586–618.

Thacker, W. C., 1976: Spatial growth of Gulf Stream meanders. *Geophys. Fluid Dyn.*, **7**, 271–295.

Williams, G. P., 1974: Generalized Eady waves. *J. Fluid Mech.*, **62**, 643–655.

——, 1975: Jupiter's atmospheric circulation. *Nature* **257**, 778.

——, 1978: Planetary circulations: 1. Barotropic representation of Jovian and terrestrial turbulence. *J. Atmos. Sci.*, **35**, 1399–1426.

——, 1979: Ultra-long baroclinic waves and Jupiter's Great Red Spot. *J. Meteor. Soc. Japan*, **57** (in press).

Williams, R. T., and J. Plotkin, 1968: Quasi-geostrophic frontogenesis. *J. Atmos. Sci.*, **25**, 201–206.